WOODHEAD PUBLISHING SERIES IN COMPOSITES SCIENCE AND ENGINEERING

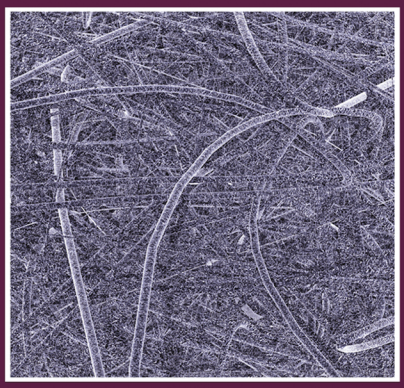

Micro and Nano Fibrillar Composites (MFCs and NFCs) from Polymer Blends

Raghvendra Kumar Mishra,
Sabu Thomas, Nandakumar Kalarikkal

WP
WOODHEAD PUBLISHING

7 Synthesis, characterization, and applications of polyolefin-polyamide micro- and nanofibrillar composites

Z.Z. Denchev, N.V. Dencheva
Institute for Polymers and Composites, University of Minho Campus of Azurém, Guimarães, Portugal

7.1 Introduction

Modern technologies require materials that are lightweight, with high mechanical strength, stiffness, flexibility, and impact resistance. At the same time, they are expected to be low in cost, friendly to automation, simple in transportation, exploitation, and recycling. Polymers in their variety—either thermoplastics or thermosets—combine to a certain extent some of these contradicting requirements. That is why polymers become more and more common, tending to limit the use or even completely substitute in many applications more traditional materials such wood, metals, and ceramics [1].

Generally, traditional neat polymers display inferior mechanical properties as compared to most ceramics and metals. Hence, to meet the constantly growing industry requirements for mechanical resistance in tension, flexion, and impact, polymers need to be reinforced, filled or otherwise modified thus producing polymer-based composites, blends, and alloys. All of these systems are multicomponent since they comprise significant amounts of two or more chemically distinct components. A large window has opened for new applications of the multicomponent polymer-based systems with the broad introduction of nanotechnologies in polymer science. The intensive research in this area showed undoubtedly that changing the type, size, shape, volume fraction, interface, and degree of dispersion or aggregation of the different components enables great amount of unique combinations of properties with high potential for successful commercial development [2].

Along with the polymer composites and blends, there exist a number of advanced, high-performance polymers such as polyimides, polyketones, polyphenylenes, the aramids, many polycarbonates, and the liquid crystalline polymers (LCP). All of them are sufficiently stiff and strong without any reinforcement but their high prices, frequently combined with difficult processing, limit their use to special applications only. Hence, for the majority of modern industries polymer-based composites do not have alternative at this point.

Micro and Nano Fibrillar Composites (MFCs and NFCs) from Polymer Blends. http://dx.doi.org/10.1016/B978-0-08-101991-7.00007-8

With respect to the size of the reinforcing component, polymer composites can be divided into: (i) *macrocomposites* comprising large-size reinforcements (e.g., glass or carbon fibers, or structures thereof), typically above 0.1 mm; (ii) *nanocomposites*, where the reinforcements have at least one of their dimensions below 100 nm and (iii) *molecular composites* reinforced by single, rigid-rod macromolecules with diameters in the angstrom range. There exist also composites with intermediate positions in this classification whose reinforcing elements have dimensions between 100 nm and 100 μm or represent bundles of macromolecules or arrays of smaller molecules. Based on the shape of the reinforcing entities, fibers, plate-like or particulate (also called tridimensional) fillers can be distinguished. By their nature these entities could be both inorganic or organic, the latter including also polymers [3].

The conventional strategy for the production of fiber reinforced polymer composites is the introduction of strong fibers into a bulk polymer matrix [4]. Systematic search for cheaper and more environmentally friendly polymer composites with superior mechanical properties led to what was called "*microfibrillar composites*" or MFC [5,6]. In view of the aforementioned classification, MFC can be considered polymer-polymer fibrous micro- or nanostructured composites. It is noteworthy that the MFC concept does not employ direct mixing of polymers with fibers. Instead, both matrix and reinforcing entities are formed in situ. In such a way, two major problems related to traditional polymer composites are resolved, namely achieving proper dispersion of the reinforcing elements and not allowing their aggregation during processing [7]. In general, MFC are prepared from properly chosen blends of thermoplastic polymers by a combination of mechanical and thermal treatments in three processing stages: (i) melt blending of the starting polymers, (ii) cold drawing of the blend followed by (iii) its selective isotropization at $T_1 < T < T_2$, where T_1 is the melting temperature of the lower-melting, matrix-forming component and T_2 is that of the higher melting one, from which the reinforcing fibrils originate.

The MFC concept was introduced in the pioneering works of Fakirov et al. [5,6]. Since then, more than two decades of development of MFC have brought forward significant results reported in many general reviews related to the processing, properties, morphology, and application of MFC produced from a number of polymer blends [1,8–13]. As repeatedly confirmed, MFC are materials with controlled heterogeneity obtainable by conventional processing techniques such as extrusion, compression molding or injection molding, with little or no agglomeration of the reinforcing phase.

Analyzing the previous studies, MFC systems can be subdivided into two major groups. The first group comprises composites prepared from *mixtures of condensation polymers*, e.g., polyester-polyamide, polyester-polycarbonate, polyester-poly (ether esters), etc. These blends are capable of self-compatibilization due to the so-called interchange reactions occurring between functional groups belonging to the matrix and reinforcements at their interface [14]. As a result, block copolymers are formed extending across the interface and linking the two MFC components chemically. This chapter is dedicated to self-compatibilizsation of MFCs.

There exist a significant number of MFC whose matrix-forming component is incapable of direct chemical reactions with the reinforcements, i.e., with no possibilities for self-compatibilization. The *polyolefin-containing* MFC belong to this second group. The obvious reason for choosing polyethylenes (high-density, HDPE, low-density,

LDPE, and linear low density, LLDPE) or polypropylene (PP) as matrix materials is related to their being cheap, abundant, and easy to process. Moreover, all PE and PP types have relatively low melting temperatures thus broadening the MFC processing window. Also, chemical bonding of the polyolefin matrix to the fibrils is possible to induce by an appropriate compatibilizer. One of the best studied microfibril-forming components within the polyolefin-containing MFC is poly(ethylene terephthalate) (PET) due to its good fiber forming capability and to the fact that PET is a major component of the plastics waste stream generated by the beverages industry. This chapter discusses Polyolefin -polyamide micro- and nanofibrillar in-situ composites.

Another group of polymers that has been considered widely as matrix components in polyolefin-based blends are the polyamides (PA). PAs are known to have high water absorption, while polyolefins are characterized by low water absorption. In addition, PAs are engineering thermoplastics of high strength, good wear resistance and heat stability that makes them useful in the automotive industry, electrical equipment manufacturing and also in the textile industry. Blending of polyolefins and PAs has been shown to be a good way to make full use of the respective advantages of both thermoplastics [15]. Transforming PE/PA blends into MFC was therefore expected to lead to materials with interesting properties. *The first goal of this chapter is to review the research on MFC systems based on PE/PA blends.*

Intensive research during the last decades revealed the big potential of the polymer-based hybrid composites. In them, a polymer matrix is reinforced by small amounts of layered clay materials, most often from the group of montmorillonites (MMT). Many thermoplastic or even thermoset polymers may be employed as matrix materials [16]. Most of the works on polymer/clay hybrids were performed with polyamides [17]. As seen from these two reviews, the PA/MMT hybrids outperform the neat polyamide in terms of mechanical strength and stiffness, thermal stability, flame retardancy, and gas barrier performance, all this at a minimal increase of the production and processing costs. Not so long time ago it was believed that polymer/clay hybrids containing 1–5 wt% nanosized loads would replace traditional glass-fiber reinforced composites with c.30 wt% of reinforcement. Unfortunately, this expectation turned to be incorrect. The main reason was the loss of mechanical performance of the industrially prepared hybrids due to agglomeration of the clay reinforcements during processing. It seemed, therefore, logical to try to obtain MFC materials with PE matrix in which the reinforcing, in situ obtained PA fibrils were additionally strengthened by nanosized MMT filler. This would be an attempt to combine the strong points of conventional fibrous composites, the LCP and clay-reinforced polymer systems, avoiding some of their most important limitations. *Therefore, it is the second goal of this chapter to review the research on such dually reinforced PE/PA microfibrillar systems.*

7.2 Polyethylene-polyamide MFC systems without nanoclay

A good knowledge of the structure and properties of polyamide/polyolefin blends is fundamental for the preparation of MFC materials on their basis. The first systematic studies of Kamal et al. on binary PE/PA immiscible blends incorporated LDPE,

LLDPE, and HDPE, and three polyamide types (PA6, PA66, and chemically modified PA66) [18]. It was found that mixing of PA with PE reduces the oxygen permeability while the water vapor permeability is increased. These changes were the strongest in the HDPE-containing blends. Notably, it is PA6 that has the lowest melting temperature, its other physical and chemical properties being comparable to PA66. Although polyamides and polyethylenes are immiscible, their blends can be successfully compatibilized in a controlled manner [15,19–25], whereby the properly compatibilized blends had sometimes better mechanical properties than the noncompatibilized. Apparently, the polymeric compatibilizers containing maleic anhydride moieties are among the best studied and the most effective [24,25].

7.2.1 Initial studies on HDPE/PA MFC

To the best of our knowledge, it was not until 2004 when the first MFC based on PE/PA blends were reported [26]. In this work we prepared oriented HDPE/PA12 blends with and without compatibilization with Yparex 8102 (YP) (commercial maleic anhydride/LLDPE copolymer) in a specially designed extruder line (Fig. 7.1) with compositions (wt%) HDPE/PA12/YP = 90/10/0 and 70/20/10. Three precursor types were produced from each blend, namely nonoriented granules (NOG) collected after the first haul-off unit, continuous oriented cable (OC), and oriented granules (OG) obtained after the final haul-off. By compression molding of various arrays of oriented precursors, MFC composites were obtained in which the HDPE matrix was reinforced by long longitudinal PA12 fibrils (LLF), bi-oriented fibrils (cross-ply) (BiF) or by short chaotically oriented fibrils (SF). Isotropic blends produced from compression molded NOG were also prepared. Scanning electron microscopy (SEM) and polarizing light microscopy (PLM) revealed the evolution of the blend morphology along

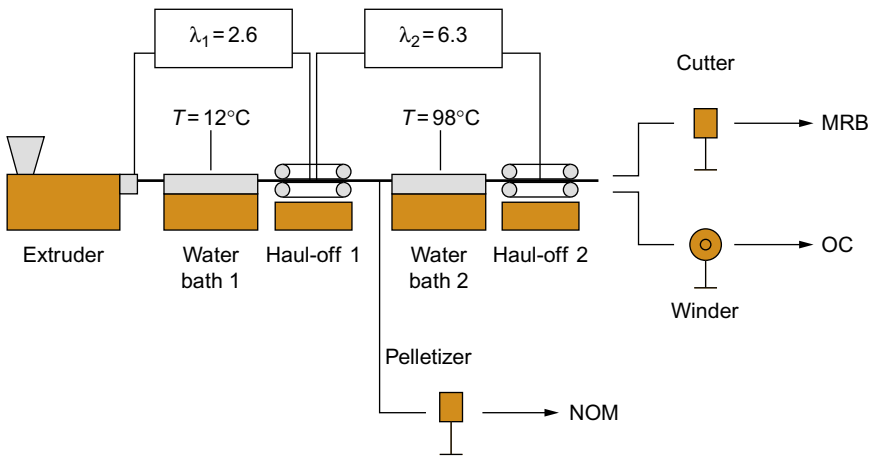

Fig. 7.1 Schematic representation of the extrusion line for preparation of MFC precursors: NOG = nonoriented blend; OC = oriented cable; OG = middle-length randomly oriented bristles; λ = draw ratio [26].

the extruder line. Microfibrils with diameters of 200–300 nm were visualized in the final MFC samples, whereby the higher the PA12 content, the larger the diameters. The mechanical tests in tension showed the best results with the LLF and BiF samples. In respect to the neat HDPE reference, these MFC showed an improvement factor IF of up to 45% for the Young's modulus E and up to 20% for the ultimate strength σ_{max}.

In the subsequent paper [27], the first synchrotron small-angle X-ray scattering (SAXS) structural studies of HPDE/PA12/YP and HDPE/PA6/YP blends were published. It was shown that the amount of YP, the draw ratio, and the temperatures of the extrusion and compression molding have a significant effect on the long spacings of the most intensive oriented SAXS reflections in the MFC samples. At this point it was still unknown that these reflections were caused by the oriented transcrystalline HDPE layer upon the polyamide fibrils. Anyway, this work showed that SAXS can be a useful tool for the structural characterization of MFC systems.

Despite these promising results, the above two works showed that the first MFC from HDPE/polyamide were very far from being optimized. The structure-properties relationship in them was not well understood. It turned to be impossible at that time to obtain noncompatibilized HDPE/PA12 MFC comprising more than 10% of highly oriented PA12 fibrils. The OC precursors with 20% and 30% of PA12 broke between the haul-off units far before all the cable had undergone neck formation along its entire length. As established later, these effects were due to nonoptimal temperatures along the extruder, bad relation between the speed of rotation of the hall-off units and weaknesses in the winder design.

Very similar effects were observed with the first HDPE/PA6/YP composites obtained somewhat later [28]. As a result of this work it was concluded that the mechanical properties of the HDPE/PA6/YP composites are controlled by several interrelated factors. The concentration of the YP compatibilizer in the starting blend was of prime importance. It enabled higher draw ratios and easier orientation of the blend precursors, but excessive YP amounts, typically above 10 wt%, deteriorated the modulus and the strength values. Furthermore, it was found that the draw ratios between the haul-off units should be kept as higher as possible to ensure proper diameters and orientation of the in situ forming PA microfibrils. And most importantly, the temperature of HDPE matrix isotropization during the compression molding and of the subsequent MFC annealing had to be very carefully controlled. By arbitrary changes in the processing parameters it was possible to obtain MFC materials with Young's modulus and tensile behavior being somehow superior to those of the HDPE matrix but a knowledge-based control of the final mechanical properties was impossible at that point.

7.2.2 Studying of the neat PA6 and PA12 reinforcement

As generally accepted, it is the reinforcing material that mostly determines the mechanical properties of a composite. Hence, the production of the HDPE/PA-based MFC that includes consecutive heating, stretching, and selective HDPE molding should be optimized in such a way so that the in situ forming highly oriented and crystalline polyamide microfibrils could have optimal stiffness and strength.

Therefore, in an attempt to understand better the influence of the drawing and heating parameters on the mechanical properties of the final MFC, systematic research on the evolution of the crystalline nanostructure in PA6 and PA12 under conditions similar to those of the MFC preparation was performed [29,30]. The relation between the crystalline nanostructure and the mechanical properties of differently prepared PA6 and PA12 samples was also assessed [31,32]

Studying the crystalline structure of PA6 by means of solid state ^{13}C NMR (SSNMR) after heating up to 200°C showed that in both isotropic and oriented samples, there was a co-existence of α- and γ-PA6 polymorphs. Close to 200°C, the α-polymorph was predominant. Annealing of oriented PA6 always caused γ- to α-form transition. These data were confirmed by synchrotron wide-angle X-ray scattering (WAXS) and further related to the mechanical properties of the respective PA6 samples. The annealing of isotropic PA6 resulted in an increase in the Young's modulus (E) and ultimate stress (σ_{max}) values, which was attributed to the observed proportional reduction of the d-spacings of the intersheet distances in both the α-PA6 and γ-PA6 polymorphs. In oriented PA6 samples, the same annealing resulted in a drastic increase in the E and σ_{max} values accompanied by a phase transition from γ-PA6 to α-PA6 and a well-pronounced reduction in the intersheet distances of both polymorphs. The stretching of the oriented samples led to an additional γ-to-α transition [31].

The crystalline structure of PA12 was studied similarly by SSNMR and X-ray scattering techniques. Isotropic and oriented PA12 displayed different ^{13}C NMR resonance lines ascribed to γ- and γ′-crystalline modifications, respectively. The isotropic γ-form and the oriented γ′-form were shown to be with hexagonal or pseudo-hexagonal crystalline lattice at room temperature. When heated, the two PA12 polymorphs demonstrated different behaviors. Above 140°C, the isotropic γ-PA12 form partially transformed into α-modification. No such transition was observed with the oriented γ′-PA12 phase even after annealing at temperatures close to melting. A γ′-γ transition was observed here only after isotropization by melting. Annealing of the PA12 oriented cables for various times in the 120°C–160°C range showed that E modulus and the σ_{max} values increased with the annealing temperature, while the elongation at break decreased. This behavior was explained by a temperature induced γ-to-α form transition and by the decrease of the intersheet distances leading to denser macromolecule packing in the crystalline domains. Similarly to what was observed with PA6, additional stress-induced γ-to-α-form transition occurred in PA12 when external stress was applied. The structural data led to the supposition of formation of a rigid amorphous phase in the annealed samples [33].

Basic method for quantifying the crystalline structure of PA6 and PA12 samples was the deconvolution of the respective SSNMR curves or linear WAXS profiles by means of peak fitting. Since it was later adopted for studying the crystalline nanostructure of the HDPE/PA MFCs it deserves a brief explanation here. Figs. 7.2A and 7.3A show typical ^{13}C NMR curves of PA6 and PA12 oriented cables, respectively. The curves were obtained under magic angle spinning (MAS) with ^{1}H-^{13}C cross-polarization (CP) and high-power ^{1}H dipolar decoupling (DD). In Figs. 7.2B and 7.3B, the respective fitted WAXS curves are presented. It can be seen that both NMR and WAXS results provide very similar data for the α- and γ-polymorph

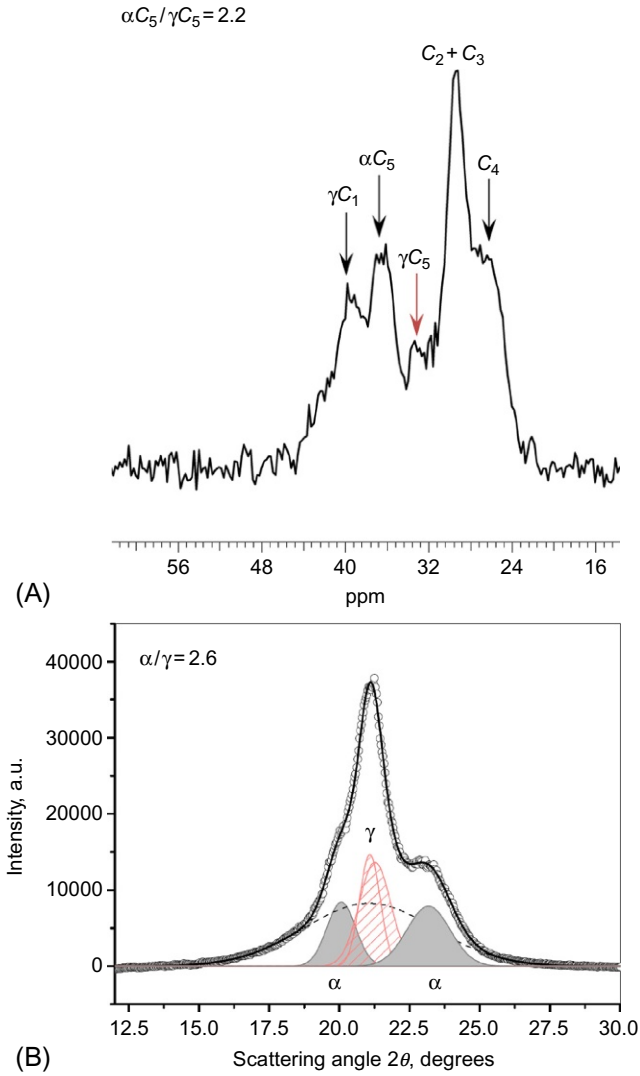

Fig. 7.2 PA6 oriented cable (OC) obtained in the extruder line of Fig. 7.1, annealed for 1 h at 200°C and characterized at 30°C by: (A) MAS/CP-DD ^{13}C NMR and (B) synchrotron WAXS. The thick solid lines represent the fit to the data points (open symbols). The peaks pertaining to α- and γ-PA6 polymorphs in 3b are shaded differently. For more details see the text. Modified from Dencheva N, Nunes T, Oliveira MJ, Denchev Z. Microfibrillar composites based on polyamide/polyethylene blends: 1. Structure investigations in oriented and isotropic PA6. Polymer 2005;46:887–901; Dencheva N, Denchev Z, Oliveira MJ, Funari SS. Relationship between crystalline structure and mechanical behavior in isotropic and oriented PA6. J Appl Polym Sci 2007;103:2242–2252.

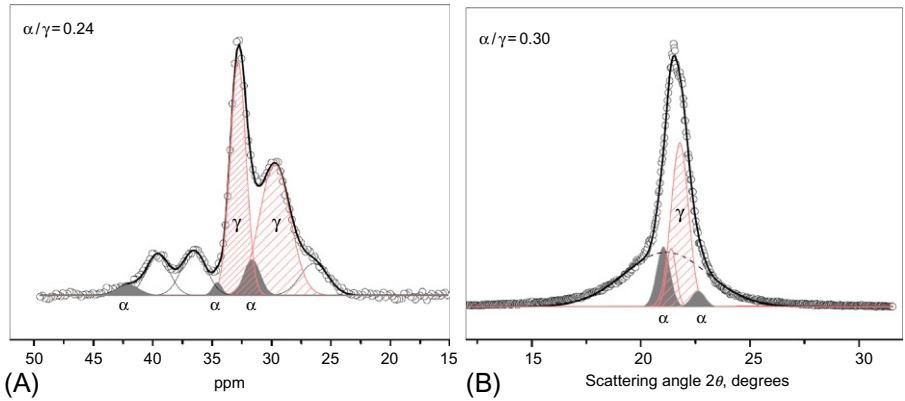

Fig. 7.3 PA12 oriented cable (OC) obtained in the extruder line of Fig. 7.1, annealed for 1 h at 160ºC and characterized at 30ºC by: (A) MAS/CP-DD 13C NMR and (B) synchrotron WAXS. The thick solid lines represent the fit to the data points (open symbols). The peaks pertaining to α- and γ-PA12 polymorphs are shaded differently. For more details see the text.
Data from Dencheva N, Denchev Z, Oliveira MJ, Nunes TG, Funari SS. Relationship between crystalline structure and mechanical behavior in oriented and isotropic PA12. J. Appl. Polym. Sci. 2008; 109:288-312.

contents in PA6 and PA12 so the combination of these two independent techniques was adopted for further structural studies in the HDPE/PA MFC systems.

Table 7.1 summarizes some structural and mechanical data of PA6 and PA12 oriented cables stretched to undergo neck formation, with or without subsequent heat treatment. It can be seen that the different annealing conditions lead to differences in the total crystallinity indexes and, more importantly, to different ratio of the α- and γ-polymorph content of the samples. In the case of PA6 oriented cables, the best mechanical response was obtained after annealing at 160°C. It led to a triplication of the *E*-values and to more than 10% improvement of σ_{max}, as compared to nonannealed PA6 samples drawn in the same way. This better mechanics can be related to a significant growth of the α/γ ratio, while the total crystallinity remained almost constant. With the PA12 oriented samples the annealing to 140°C and 160°C also caused a growth of the values of *E* and σ_{max} accompanied by a very slight increase of the α-PA12 content. It can be therefore concluded that the best mechanical properties of the polyamide reinforcements are revealed at their maximum stretching followed by a prolonged annealing in the140°C–160°C range. Interestingly, while the stiffness of the PA6 oriented samples can be clearly better than that of PA12 with similar heat and mechanical treatment, the tensile strength of the latter can be notable better. This was an important indication for designing the MFC compositions and the conditions for their processing, namely the melt-mixing and compression molding temperatures and duration.

Table 7.1 Relation between structural characteristics and mechanical properties in differently annealed oriented PA6 and PA12

Sample and annealing conditions		WAXS crystallinity index, (%)	α/γ	Young's modulus E, (GPa)	Ultimate strength σ_{max}, (MPa)	Strain at break ε_{br}, (%)
Oriented PA6 (OC)	No annealing	48.3	0.59	0.99 ± 0.04	201 ± 17	150 ± 68
	1 h/120°C	47.2	0.66	1.78 ± 0.12	169 ± 19	74 ± 20
	1 h/160°C	47.9	1.05	3.18 ± 0.14	223 ± 14	69 ± 14
	1 h/200°C	54.6	2.38	3.78 ± 0.17	185 ± 10	48 ± 10
Oriented PA12 (OC)	No annealing	41.8	0.25	1.63 ± 0.08	241 ± 10	27 ± 3
	1 h/120°C	51.1	0.36	1.46 ± 0.10	216 ± 8	21 ± 2
	1 h/140°C	52.6	0.34	2.19 ± 0.12	266 ± 10	22 ± 2
	1 h/160°C	49.3	0.30	2.24 ± 0.15	234 ± 8	20 ± 1

Modified from Dencheva N, Denchev Z, Oliveira MJ, Nunes TG, Funari SS. Relationship between crystalline structure and mechanical behavior in isotropic and oriented PA12. J Appl Polym Sci 2008;109:288–302; and Dencheva N. Development and investigation of novel in-situ reinforced nanocompo-sites based on oriented polymer blends [Ph.D. thesis]. University of Minho; 2008. https:/repositorium.sdum.uminho.pt/bitstream/1822/9020/1/Dencheva_N%20Binder%201.pdf.

7.2.3 Structure-properties relationship in HDPE/PA MFC without clay

The systematic studies on the structure-properties relationship in polyamides after combined mechanical and thermal treatment enabled knowledge-based optimization of the MFC processing toward increased mechanical properties in tension, impact, and flexion. For full details of this process the reader is encouraged to consult the doctoral dissertation on HDPE/polyamide MFCs [33], and the subsequent articles dedicated to various aspects of the preparation, mechanical behavior, structure, and morphology of HDPE/PA6 [34,35] and HDPE/PA12 [36] compatibilized and noncompatibilized MFC without other fillers. A book chapter [37] summarizing the accomplishments in this area appeared encompassing the state-of-the-art until 2012. In the present chapter only the most important findings described in that series of works will be discussed.

7.2.3.1 Mechanical properties

The optimization started with redesigning the stretching line used to produce the oriented HDPE/PA precursors. Fig. 7.4 shows the newly designed stretching line comprising three haul-off rolls (pos. 3, 5, and 7) and a winding device (pos. 8). An additional hot air oven (pos. 6) was necessary to maintain the temperature of the stretched blend well above the T_g of the polyamide, typically in the 80°C–90°C range. This configuration allowed high orientation of the HDPE/PA blend through neck formation without mechanical failure of the cable which was quite often with the initial stretching line in Fig. 7.1. Moreover, MFC precursors with 20% and 30% of polyamide were possible to produce and orient.

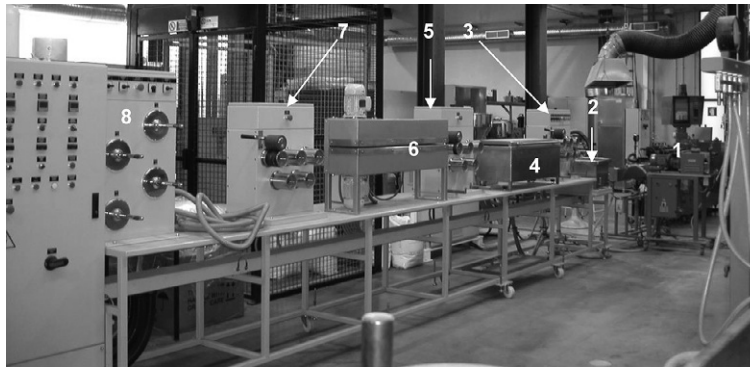

Fig. 7.4 Optimized stretching line used for preparation of MFC precursors: 1, laboratory extruder; 2, first water bath; 3, first haul-off rolls; 4, second water bath; 5, middle haul-off rolls; 6, hot air oven; 7, final haul-off rolls; 8, multiaxes winder.

In the new stretching line the typical precursor preparation starts with drying the corresponding premixed amounts of granulates of the matrix and reinforcing materials at 90°C. Right after the die the extrudate is cooled in the first water bath to 10°C–12°C. Meanwhile, the first haul-off unit applies a slight drawing stabilizing the line velocity and the extrudate cross-section. Further drawing is performed in the second and third haul-off units, after heating the extruded strand in the second water bath above 95°C. The total draw ratio achieved was $\gamma = 16$ causing the diameters of the strands to decrease from 2.5 mm to 0.5–0.8 mm. At the exit of the last haul-off device the HDPE/PA blend is in the form of oriented cable (OC). The latter could be cut to middle-length, randomly oriented bristles (MRB). Nonoriented granules of each blend were also obtained by pelletizing of extrudate obtained after the first haul-off (NOG). The final MFC were obtained after selective melting and isotropization of the HDPE matrix material and its controlled crystallization carried out in a hot press at a typical temperature of 160°C and a pressure of 10–15 MPa followed by cooling at 10°C/min. More details about the sample preparation can be found elsewhere [34–36].

Table 7.2 summarizes the composition and type of all composite materials obtained from HDPE/PA polymer blends. The term "unidirectional ply," UDP denotes a MFC plate (called also "lamina") obtained by hot pressing of parallel bundles of OC whose lengths coincide with the length of the plate. The term "cross-ply composite," CPC denotes MFC laminate obtained by hot-pressing of two mutually perpendicular arrays of OC bundles trying to maintain the same density of the reinforcing elements along the two dimensions of the final MFC laminate plate. NOM and MRM were obtained by compression molding of NOG or MRB, respectively. It should be noted that the UDP samples are fully anisotropic, i.e., their properties will vary according to the direction from a point because the continuous PA fibrils are embedded in the isotropic HDPE matrix with strict uniaxial alignment. Meanwhile, the MRM and NOM systems

Table 7.2 Composition of the MFC precursors, extrusion temperatures and composite types

HDPE/PA6/YP	HDPE/PA12/YP
90/10/0 80/20/0 70/20/10 75/20/5 77.5/20/2.5 65/30/5	90/10/0 80/20/0 70/20/10 75/20/5 77.5/20/2.5 65/30/5
Extrusion temperature (°C)	
250°C	210°C
Composite type	
UDP,CPC,NRM,NOM	UDP,CPC,NRM,NOM

UDP, unidirectional ply; *CPC*, cross-ply composite; *MRM*, composite obtained from middle-length, randomly arranged bristles; *NOM*, non-oriented material obtained from NOG; YP is the compatibilizer Yparex (DSM). The compositions of the samples are in wt.%.

are expected to behave isotropically since the PA reinforcing elements (rods and spheres, respectively) are randomly aligned within the matrix [33].

It is important to note that the mechanical properties of the MFCs can depend on the way the isotropization was achieved. As found out previously, the compression molding route toward MFC, in contrast to injection molding, allows staying accurately within the required temperature processing window that preserves the fibrillar morphology of the fibril-forming material during the isotropization stage [38]. In addition, compression molding permits the preparation of MFC from oriented precursors in the form of UDP laminae or laminates with different plate geometries. Conversely, injection molding can only use NOG or MRB precursors to get matrices reinforced by either isotropic entities or short, randomly oriented micro- or nanofibrils. With all these ideas in mind, compression molding was selected as the method for matrix isotropization in HDPE/PA/YP MFCs.

Since the UDP lamina represents the basic building block in long fiber reinforced composites [39], the mechanical characterization in tension started with UDP materials reinforced by either PA6 (Fig. 7.5A) or PA12 (Fig. 7.5B) microfibrils, the stress being applied parallel to the fibrils' alignment. Fig. 7.5 depicts the resulting stress-strain curves. Their visual inspection shows very similar tensile behavior irrespective of the polyamide reinforcement. With the exception of the two 90/10/0 samples with only 10% of polyamide reinforcements (curves 2), all other MFC materials show notable increase in σ_{max} and a drop in the ε_{br} values along with the disappearance of clear yield point, as compared to the neat HDPE (curves 1). This is typical for the

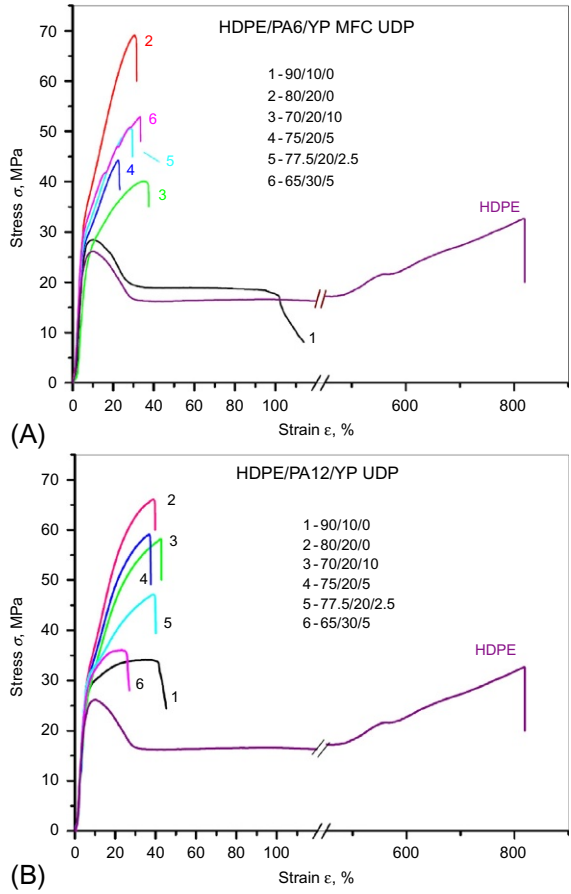

Fig. 7.5 Representative stress-strain curves of unidirectional ply (UDP) MFC reinforced by PA6 (A) and PA12 (B) fibrils. The curve of the neat HDPE matrix is shown for comparison.

conventional fiber-reinforced composites. It should be noted that the UDP material performed in tension better than MRM and much better than NOM [37].

Fig. 7.6A and B compare the E and σ_{max} values for all HDPE/PA6 materials with best improvement factors of 33% and 120%, respectively. Notably, the composites with the biggest concentration of compatibilizer YP showed the smallest enhancement of the tensile properties. Meanwhile, the improvement of the E modulus in the HDPE/PA12/YP samples was in the range of 10%–30%, while the tensile strength reached 150% in respect to the HDPE matrix (Fig. 7.6C and D). The negative effect of YP on the mechanical properties is less obvious as compared to the PA6-reinforced MFC. The rule of mixtures can be used to predict the tensile behavior of both types of UDP samples. According to Fig. 7.6, the experimental values for stiffness and strength in MFC without compatibilizer displayed positive deviations from those predicted

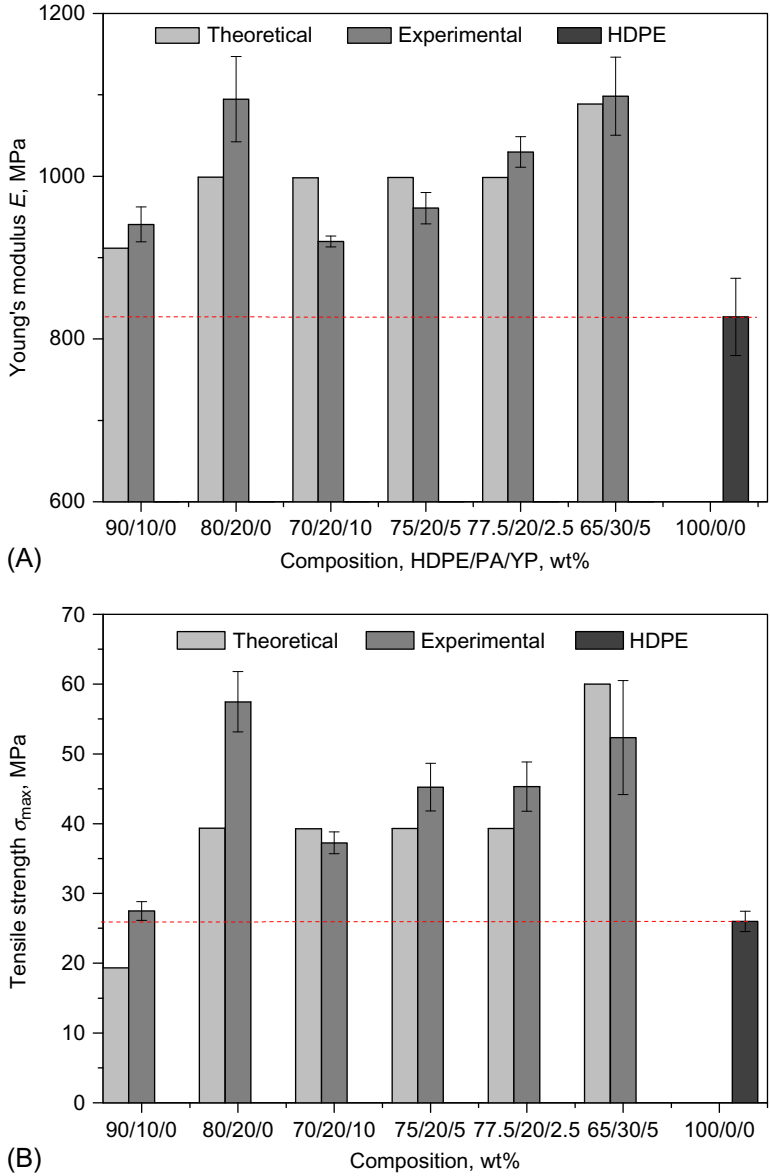

Fig. 7.6 Theoretical and experimental tensile properties in unidirectional ply (UDP) MFC containing: PA6 (A, B) or PA12 (C, D) reinforcing fibrils. σ_{max} = longitudinal tensile strength; E = longitudinal Young's modulus. Theoretical predictions made on the basis of the rule of the mixtures [39]. The HDPE matrix values are also presented for comparison.
Modified from Denchev Z, Dencheva N. Preparation, mechanical properties and structural characterization of in-situ microfibrillar composites based on oriented polyethylene/polyamide blends. In: Fakirov S, Bhattacharya D, editiors. Synthetic polymer-polymer composites. Hanser Fachbuch; 2012. p. 465–522.

Continued

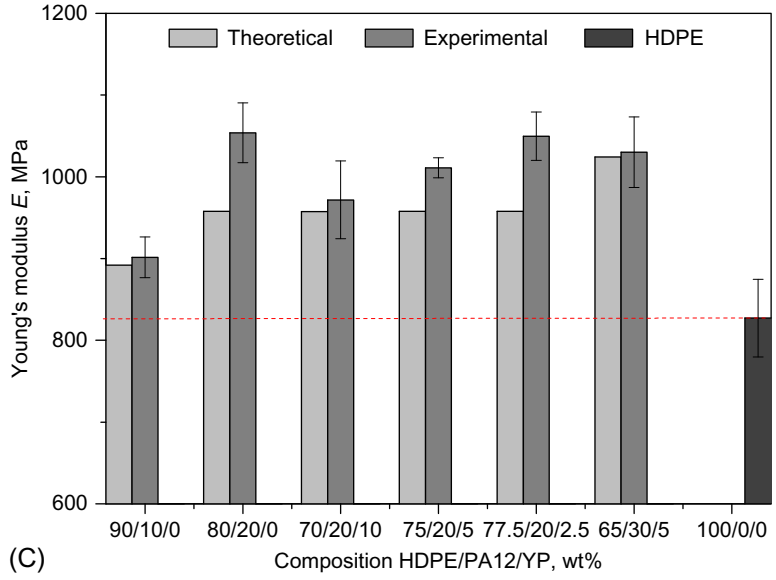
Theoretical
Experimental
HDPE
Young's modulus E, MPa
1200
1000
800
600
90/10/0
80/20/0
70/20/10
75/20/5
77.5/20/2.5
65/30/5
100/0/0
Composition HDPE/PA12/YP, wt%
(C)

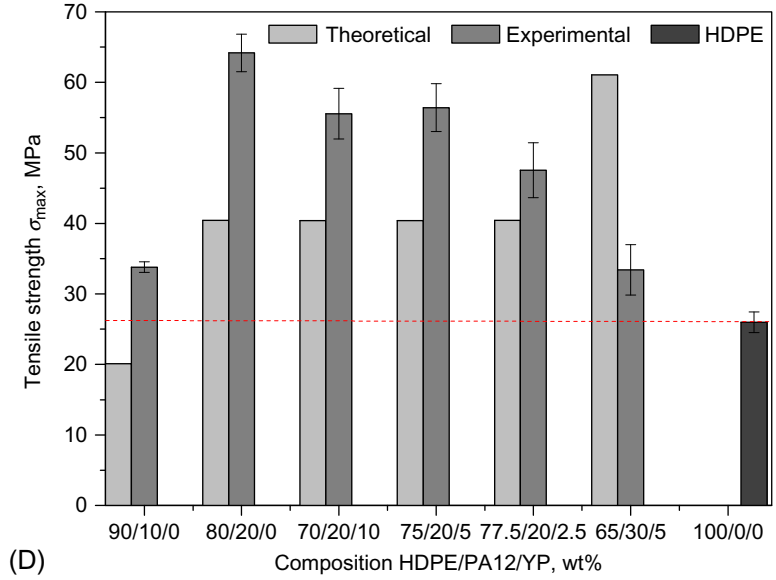
Theoretical
Experimental
HDPE
Tensile strength σmax, MPa
70
60
50
40
30
20
10
0
90/10/0
80/20/0
70/20/10
75/20/5
77.5/20/2.5
65/30/5
100/0/0
Composition HDPE/PA12/YP, wt%
(D)

Fig. 7.6, cont'd

theoretically, being of c.10% for E and 50%–70% for σ_{max}. As it will be indicated further in the text, these deviations may be related to the thickness and geometry of interfacial layers between the fibril and matrix.

It should be noted that the above improvements in the tensile properties of the anisotropic UDP materials are observed only along the axis of the reinforcing fibrils. Testing the UDP laminas perpendicularly to the fiber direction produces E and σ_{max} values comparable to those of the neat HDPE matrix, i.e., about 0.8 GPa and 26 MPa. For some noncompatibilized PA-reinforced systems, the values were even lower.

Polymer materials are applied as molded plates or laminate composite products. They must be strong and stiff, not only in tension, but principally in flexural and impact modes in order to perform as designed. Therefore, the flexural stiffness C_R and the impact resistance of all MFC materials were assessed as a function of the composition and reinforcement type. To avoid the effects of anisotropy in UDP samples, CPC, MRM, and NOM were studied applying a three-point support flexural test according to Nunes et al. [40] and instrumented falling weight impact test [35].

The three-point flexural test is perhaps the only one where both PA6- and PA12 MFC materials undoubtedly showed better performance in all compositions under investigation in the form of CPC, MRM, and NOM (Fig. 7.7). Irrespective of the orientation and alignment of the reinforcing constituent, all samples display notably better flexural stiffness as compared to the HDPE, even with the lowest polyamide content. Although there is no big difference in the flexural behavior of the CPC, MRM, and NOM composites, those with oriented polyamide component, either PA6 or PA12, perform better. As a whole, the PA12 containing composites showed better flexural behavior, keeping higher values in all systems studied. The improvement varies in the range of 60%–180% for the PA12 laminates and between 50% and 90% for the PA6 laminates. From all compositions the best performing composite was based on PA12 65/30/5 CPC that displays a flexural stiffness of 4.2 GPa, which is 2.8 times higher than the respective HDPE value.

Fig. 7.8 compares the data from the impact tests: the peak and the total impact energies per unit thickness of PA6- and PA12 CPC, MRM, and NOM composites. The data are quite heterogeneous and do not suggest clear trends. Nevertheless, as regards the CPC systems (Fig. 7.8A), PA12 reinforcement leads to improvement of the peak energy values, which are higher than the HDPE and the respective PA6 compositions. This means that the PA12 reinforcement in the CPC laminates works better as far as the peak energy is concerned. However, in respect to the total energy (Fig. 7.8B) the comparison with PA6 is not so clearly in favor of PA12. The PA6 systems without (80/20/0) or with low YP concentrations (77.5/20/2.5) are better than the equivalent PA12 reinforced composites. The same considerations are valid also for the MRM composites with PA6 and PA12 (Fig. 7.8C and D), although the peak and total energies here are lower than the respective CPC composites. In most of the MRM compositions the two energies are close or lower than HDPE matrix. The absence of orientation of the reinforcing component (Fig. 7.8E and F) leads to a considerable decline of the toughness in both PA6 and PA12 NOM systems. A clear indication of these experiments is that the full potential of the PA6 and PA12-MFCs in impact

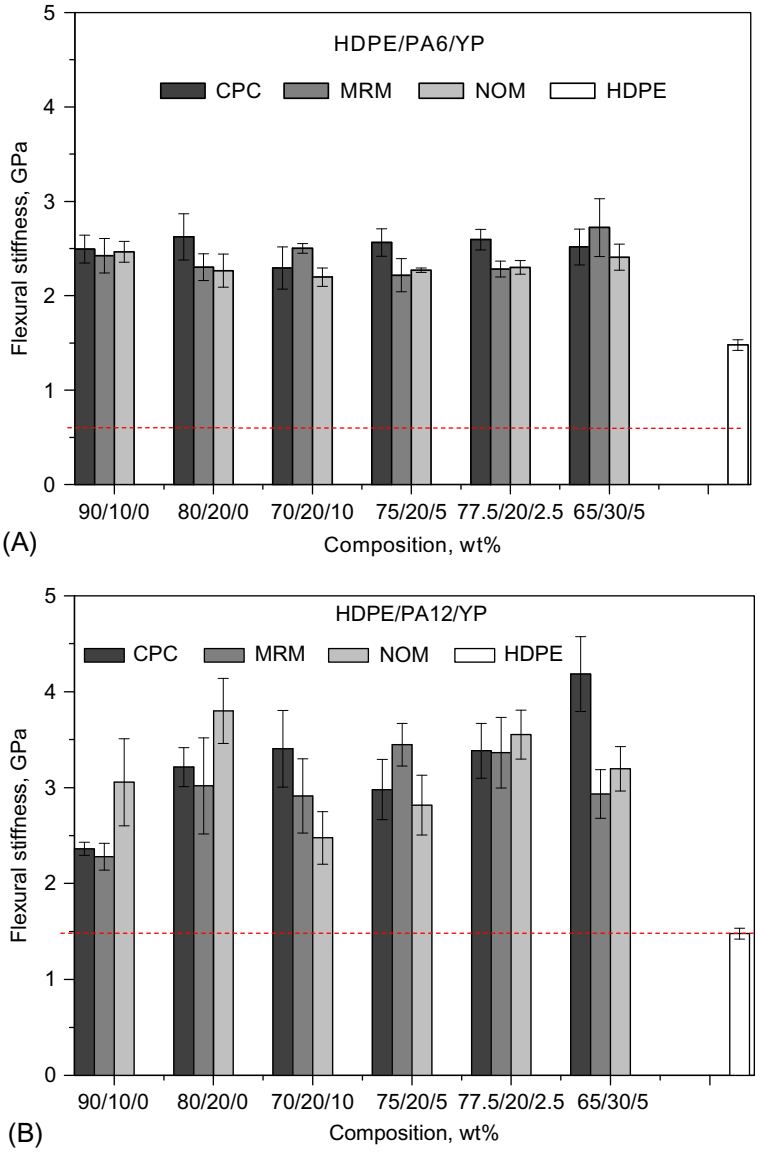

Fig. 7.7 Comparative chart of the flexural stiffness of all HDPE/PA6/YP (A) and HDPE/PA12/YP (B) composites studied.
Modified from Denchev Z, Dencheva N. Preparation, mechanical properties and structural characterization of in-situ microfibrillar composites based on oriented polyethylene/polyamide blends. In: Fakirov S, Bhattacharya D, editiors. Synthetic polymer-polymer composites. Hanser Fachbuch; 2012. p. 465–522.

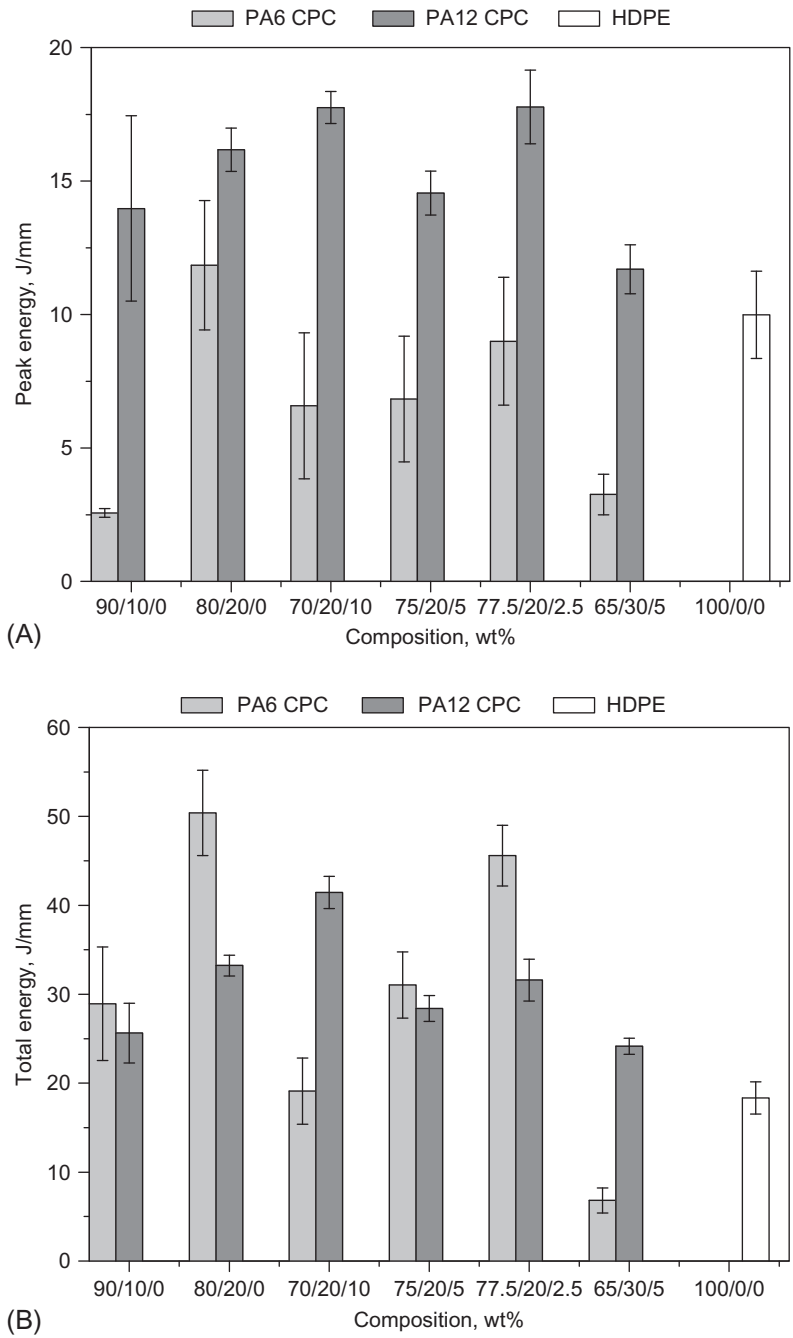

Fig. 7.8 Comparative Impact test of HDPE/PA6/YP and HDPE/PA12/YP composites: (A, B) peak and total energies of CPC;

Continued

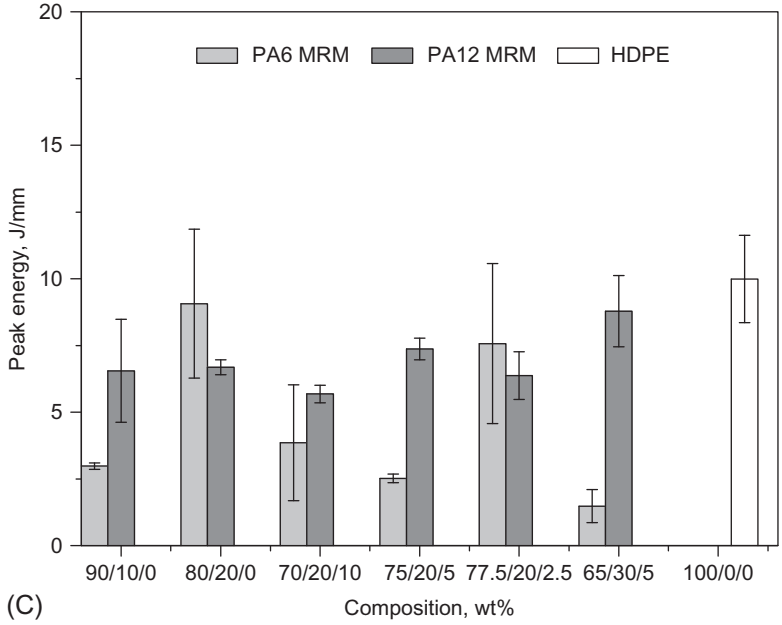

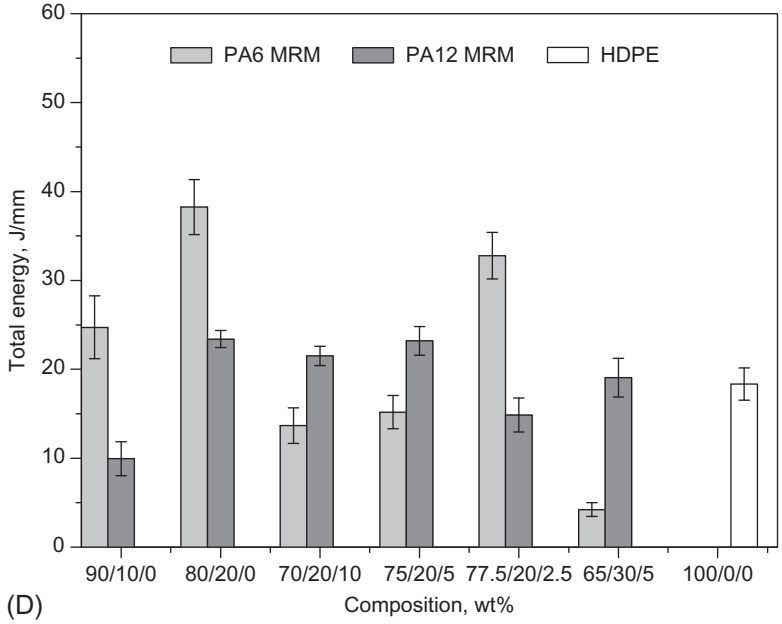

Fig. 7.8, cont'd (C, D) peak and total energies of MRM;

Continued

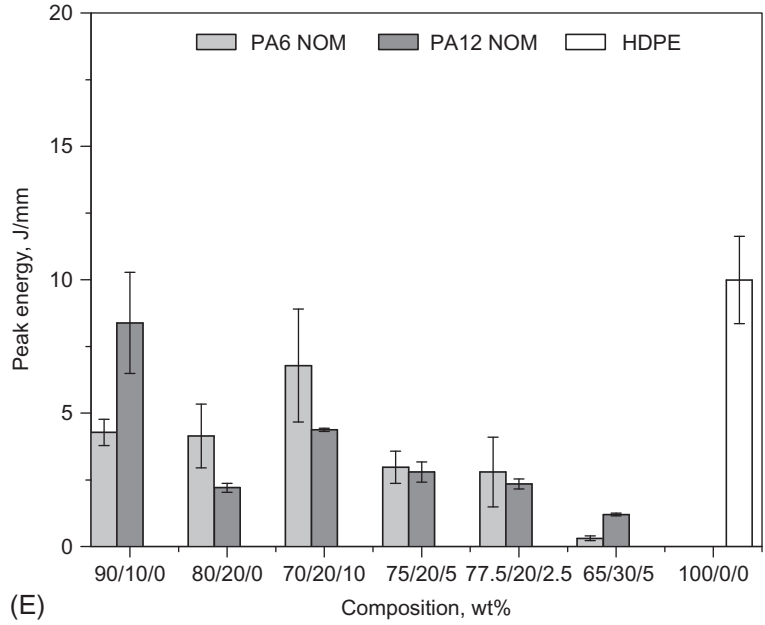

(E)

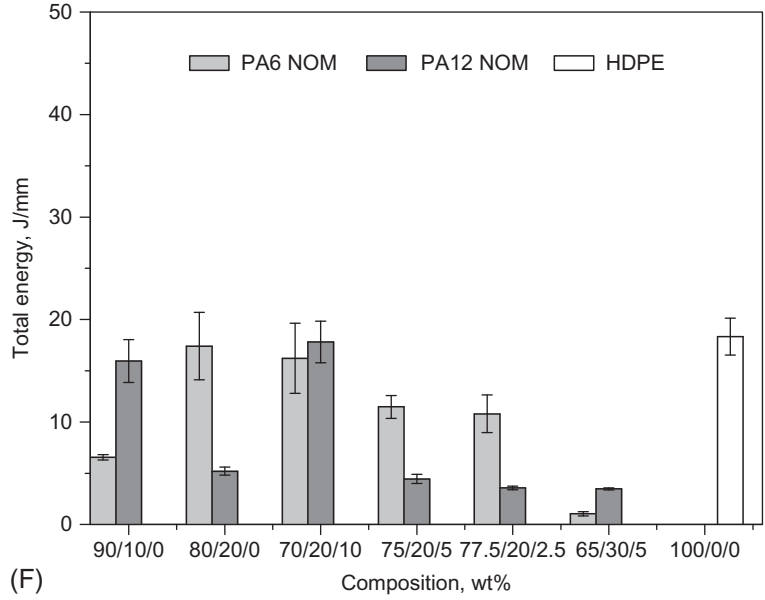

(F)

Fig. 7.8, cont'd (E, F) peak and total energies of NOM.
Modified from Denchev Z, Dencheva N. Preparation, mechanical properties and structural characterization of in-situ microfibrillar composites based on oriented polyethylene/polyamide blends. In: Fakirov S, Bhattacharya D, editiors. Synthetic polymer-polymer composites. Hanser Fachbuch; 2012. p. 465–522.

is only reached when the material is used in the form of laminates with proper ply alignment.

Very recent studies of Liu et al. [41] on the mechanical properties of HDPE/PA6 MFC materials compatibilized with three different compatibilizers based on maleinized PE, maleinized butylacrylate/PE copolymer, and glycidyl methacrylate-functionalized PE revealed a positive effect of the compatibilizers on the mechanical properties in tension, flexure, and impact. This conclusion is contrary to the results in Figs. 7.6–7.8. This should be attributed to the fact that Liu et al. prepared their MFC by hot stretching and final injection molding, whereas in our studies cold drawing to continuous OP combined with their compression molding to CPC was used. Therefore, any direct comparison of the mechanical behavior of MFC in both cases is not straightforward.

7.2.3.2 Morphological studies

Summarizing the results from the mechanical characterization of the HDPE/PA6/YP and HDPE/PA12/YP composites, it can be concluded that the improvement of the Young's moduli of the anisotropic UDP MFCs reinforced by unidirectionally aligned fibrils were in the range of 30% for both PA6 and PA12, while the tensile strength grew with 120% (PA6) and 150% (PA12) in respect to the HDPE matrix. The tensile properties of the UDP composites in transverse direction were close to or slightly higher than HDPE. As a rule, all anisotropic composites with the biggest concentration of compatibilizer YP showed the smallest enhancement of the tensile properties. Analogously, the best flexural stiffness was achieved in the absence of or at low concentration of YP, the improvement factor IF being of 75%–80% for best PA6-reinforced CPC composites, reaching 130% for PA12 reinforcement.

Interestingly, similar or sometimes even better mechanical performance of the PA12-reinforced MFC materials was observed in the above tests. Having in mind the data in Table 7.1 comparing the tensile characteristics of oriented and annealed PA6 and PA12, this finding seems to be logical. The supposed absence of fibrillar morphology of the reinforcing component (i.e., no MFC structure present as in NOM) or high amount of compatibilizer led to poor mechanical properties of the final composite. Therefore, the explanation of the reinforcing effect should be related in the first place with *proving and characterizing the fibrillar morphology* of the MFC reinforcements. On the other hand, the last step of the MFC production cycle involves nonisothermal crystallization of the selectively molten matrix in the presence of the oriented and crystalline PA fibrils with diameters from several hundred nanometers to several micrometers. As repeatedly demonstrated [42], under such thermal conditions heterogeneous nucleation can occur with sufficiently high density along the interphase region leading to the formation of layers of matrix material around the fiber, known as *transcrystallinity* (TC) or *transcrystalline layers* (TCL). This phenomenon was also investigated in relation to mechanical performance.

The first extensive SEM investigation of MFC and their precursors performed by Evstatiev et al. [43] undoubtedly showed the fibrillar structure of the PET

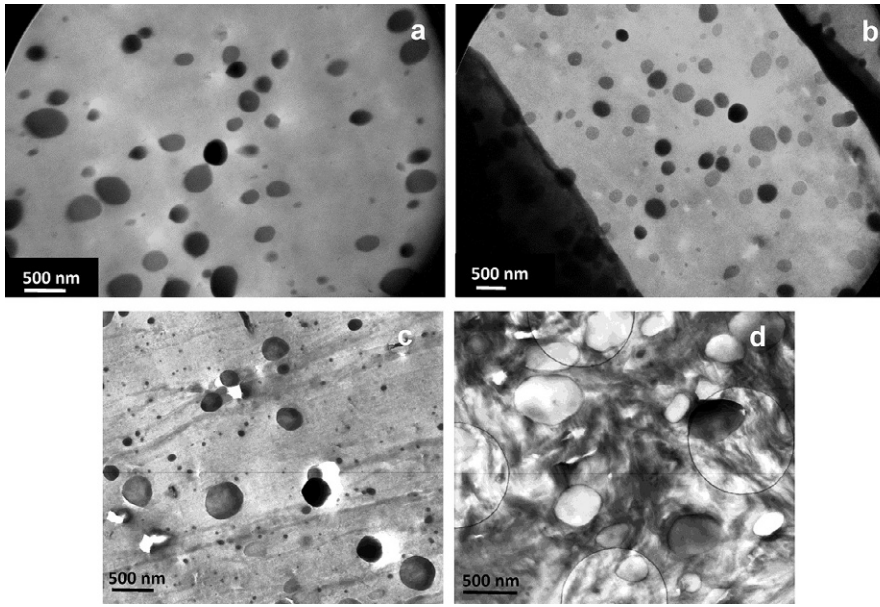

Fig. 7.9 TEM images of selected oriented cables OC and MFC: (A) OP HDPE/PA12/YP = 80/20/0; (B) OP HDPE/PA12/YP = 70/20/10; (C) OP HDPE/PA6/YP = 80/20/0; (D) MFC HDPE/PA6/YP = 80/20/0 [44].

reinforcements preserved after the PA6 matrix isotropization. Since then, electron microscopy has been used to visualize the orientation and morphology of the matrix and reinforcing components in almost every report on MFC. Our own results [37,44] on visualization of the morphology of HDPE/PA MFC by SEM and TEM indicated that sample preparation by ultramicrotoming of the OC precursors and MFC is extremely difficult, due to their hardness and brittleness. Acceptable TEM images were produced only in few cases (Fig. 7.9), displaying cuts normal to the uniaxially arranged polyamide fibrils. For OC samples, almost circular cross-sections are observed with diameters in the 350–450 nm range for the PA12-containing OC (Fig. 7.9A and B) and up to 500 nm for the one with PA6 (Fig. 7.9C). The fibrils' cross-sections in the MFC with HDPE/PA6/YP = 80/20/0 (Fig. 7.9D) display lesser roundness but their average diameters are the same as in the respective OC.

Sample preparation for the SEM studies by cryogenic fracture was possible for all MFC samples. The images obtained allowed the assessment of the microfibrils' visible average diameters (Fig. 7.10): 700–765 nm for the PA6-containing MFC (Fig. 7.10A and B), 500–600 nm for MFC with PA12 reinforcement (Fig. 7.10C and D). Notably, the diameters of the fibrils in OC precursors are significantly lower than the visible diameters of the fibrils after melting/recrystallization of the HDPE matrix during the MFC formation. Bearing in mind the above-mentioned selective melting and recrystallization of HDPE matrix in the presence of crystalline and highly oriented polyamide reinforcing component, it may be therefore supposed that the

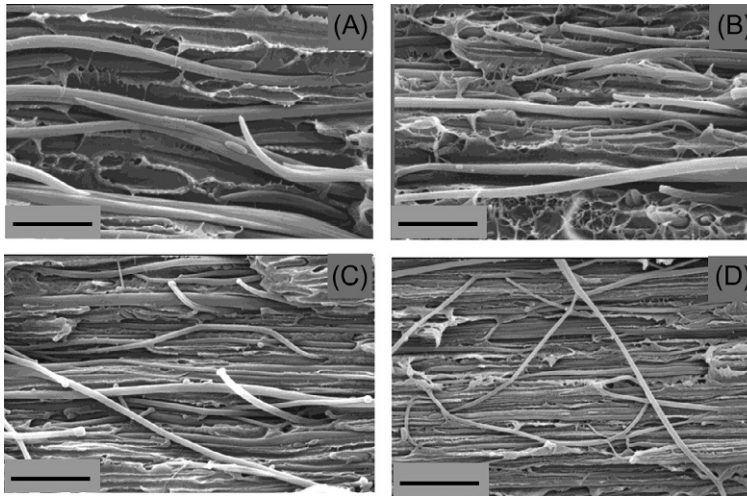

Fig. 7.10 Selected SEM images of MFC: (A) HDPE/PA6/YP = 80/20/0; (B) HDPE/PA6/YP = 70/20/10; (C) HDPE/PA12/YP = 80/20/0; (D) HDPE/PA12/YP = 70/20/10. The scale bar in the images corresponds to 5 μm.
Modified from Dencheva N, Stribeck A, Denchev Z, Nanostructure development in multicomponent polymer systems and its characterization by X-ray scattering. Eur Polym J 2016;81:447–469.

microfibrils in Fig. 7.10 should have a polyamide core covered by a TCL of HDPE. Any other process capable to contribute to thickening of fibrils (e.g., relaxation during compression molding) can be ruled out since the diameters of the PA6 fibrils observed by TEM in OC and after MFC formation by compression molding are basically the same (Fig. 7.9C and D).

As seen in Figs. 7.9 and 7.10, neither TEM nor SEM technique provides direct visualization of the TCL in HDPE/PA/YP systems. In fact, there exist very few direct proofs of transcrystallinity in MFC. Friedrich et al. [45] reported a TEM image of a PET/LDPE = 50/50 MFC showing the cross-section of a PET microfibril covered by TCL of LDPE with thickness of about 150 nm. TCL was observed directly by AFM in a iPP/PET = 85/15 MFC obtained by slit extrusion [46]. To the best of our knowledge, this has not been succeeded so far in HDPE/PA6 MFC due to the already mentioned ultramicrotoming issues.

7.2.3.3 Combined microscopy and X-ray studies

As confirmed by morphological studies, the HDPE/PA MFC comprises oriented polyamide fibrils embedded in an isotropic HDPE matrix. These fibrils are covered by HDPE matrix material that, having in mind the genesis of TCL [42], is most probably also oriented. This coaxial morphology provides a possibility of indirect quantification of the TCL in MFC by scattering techniques. From the theory of the X-ray scattering it is known that if a semicrystalline polymer sample contains oriented and

nonoriented domains, the total scattered intensity could be considered a superposition of anisotropic and isotropic scattering that can be separated by 2D deconvolution [47]. The azimuthally dependent anisotropic part of the scattering $\Phi_{aniso}(s,\chi)$ that arises from the oriented domains of the sample can be computed subtracting from the total scattering $\Phi(s,\chi)$ the azimuthally independent, isotropic scattering Φ_{iso} (s):

$$\Phi_{aniso}(s,\chi) = \Phi(s,\chi) - \Phi_{iso}(s) \tag{7.1}$$

where χ is the azimuthal angle. This procedure allows for separation of the matrix HDPE and PA6 fibrils peaks, as well as distinction between the oriented and isotropic HDPE from TCL and MFC matrix, respectively.

To elucidate the morphology and microstructure of both fibrils and matrix of the MFC samples, static synchrotron WAXS patterns at 30°C were obtained (Fig. 7.11). The total WAXS of a typical PA6-reinforced MFC sample (Fig. 7.11A) shows that the crystallographic characteristics of HDPE and PA6 are very similar with a strong overlapping of the respective reflections. The total WAXS pattern of PA12-containing

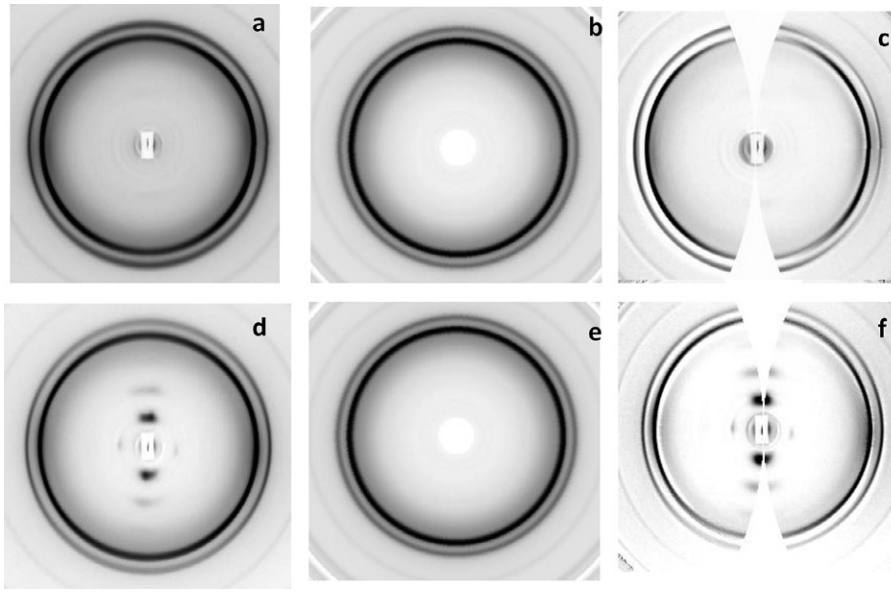

Fig. 7.11 Example of separation of the total WAXS ($\Phi(s,\chi)$) at 30°C into oriented intensity $\Phi_{aniso}(s,\chi)$ and isotropic intensity $\Phi_{iso}(s)$ for two MFC samples: PA6-reinforced (A–C) and PA12-reinforced (D–F) with composition HDPE/PA/YP = 80/20/0: Left, $\Phi(s,\chi)$; Center, $\Phi_{iso}(s)$; Right, $\Phi_{aniso}(s,\chi)$. Fiber direction is vertical.
From Dencheva N, Denchev Z, Oliveira MJ, Nunes TG, Funari SS. Relationship between crystalline structure and mechanical behavior in isotropic and oriented PA12. J Appl Polym Sci 2008;109:288–302; and Dencheva N, Oliveira MJ, Carneiro OS, Pouzada AS, Denchev Z. Preparation, structural development, and mechanical properties of microfibrillar composite materials HDPE/PA6 oriented blends. J Appl Polym Sci 2010;115:2918–2932.

MFC (Fig. 7.11D) reveals meridional (i.e., on the vertical of the pattern) point-like reflections of the γ(020) PA12 crystalline planes. These reflections were observed by us previously and suggest considerable orientation of the PA12 reinforcing fibrils (*b*-axis is the fiber axis) [32]. Similar γ(020) meridional reflections appear in highly oriented neat PA6 [29] but in the respective MFC they can be missing [34]. The previously discussed studies on the neat oriented polyamides show that the PA6 microfibrils contain less γ-polymorph as they become less oriented than the PA12 microfibrils during the OC formation due to the better ductility of PA12.

Subtracting the nonoriented WAXS $\Phi_{iso}(s)$ that characterizes the isotropic matrix (Fig. 7.11B and E) from the total WAXS $\Phi(s,\chi)$ (Fig. 7.11A and D) for both samples in Fig. 7.11 reveals clearly the oriented WAXS $\Phi_{aniso}(s,\chi)$ that bears the structural information for the oriented reinforcing fibrils (Fig. 7.11C and F). From the last two images of Fig. 7.11, it can be concluded that a significant part of the HDPE matrix is able to crystallize aligning along the PA6 and PA12 fibrils thus forming an oriented TCL in such a way that the chain directions of the two polymers coincide. The rest of the matrix HDPE situated away from the PA fibrils crystallizes isotropically.

The linear profile of the isotropic WAXS intensity $\Phi_{iso}(s)$ can readily be separated into distinct peaks in order to detect its crystallographic components. This is not the case for the anisotropic WAXS intensity $\Phi_{aniso}(s,\chi)$. Thus, for the mere purpose of component detection by peak separation from each anisotropic WAXS we computed curves according to Eq. (7.2):

$$\Phi_{aniso}(s) = \int_0^{\pi} \Phi_{aniso}(s,\chi)d\chi \tag{7.2}$$

that were afterwards fitted by Gaussian peaks. The reason for this simple conversion is the fact that the strict intensity isotropization cannot be performed because our oriented WAXS data are incomplete. For completion we should have measured the patterns of samples in the same state under different tilt angles and combine them into a complete view of the reciprocal space. This is extremely time-consuming considering both the measuring experiments and the mathematical treatment.

The results from peak-fitting of the $\Phi_{aniso}(s)$ for three representative MFC samples are shown in Fig. 7.12A–C. For the HDPE/PA6 system with 20 wt% of PA6, the oriented WAXS clearly shows the (110), (200) and (210) contributions of the HDPE and also the crystalline reflections of oriented α- and γ-PA6 polymorphs (Fig. 7.12A). The same processing was performed with the oriented WAXS of a HDPE/PA12 and a HDPE/PA6-MMT composite (Fig. 7.12B and C). In all cases, HDPE peaks were found in the oriented WAXS, along with the typical reflections for α- and γ-polyamide phases. As expected, peak fitting of the nonoriented WAXS showed presence of crystalline HDPE only (Fig. 7.12C). For a good fit in this last case two diffuse peaks were necessary that should be attributed to the amorphous isotropic HDPE matrix and the amorphous fraction of the polyamide microfibrils. As previously postulated [47], the oriented WAXS should not require the introduction of amorphous halo, which was the case in Fig. 7.12A and B.

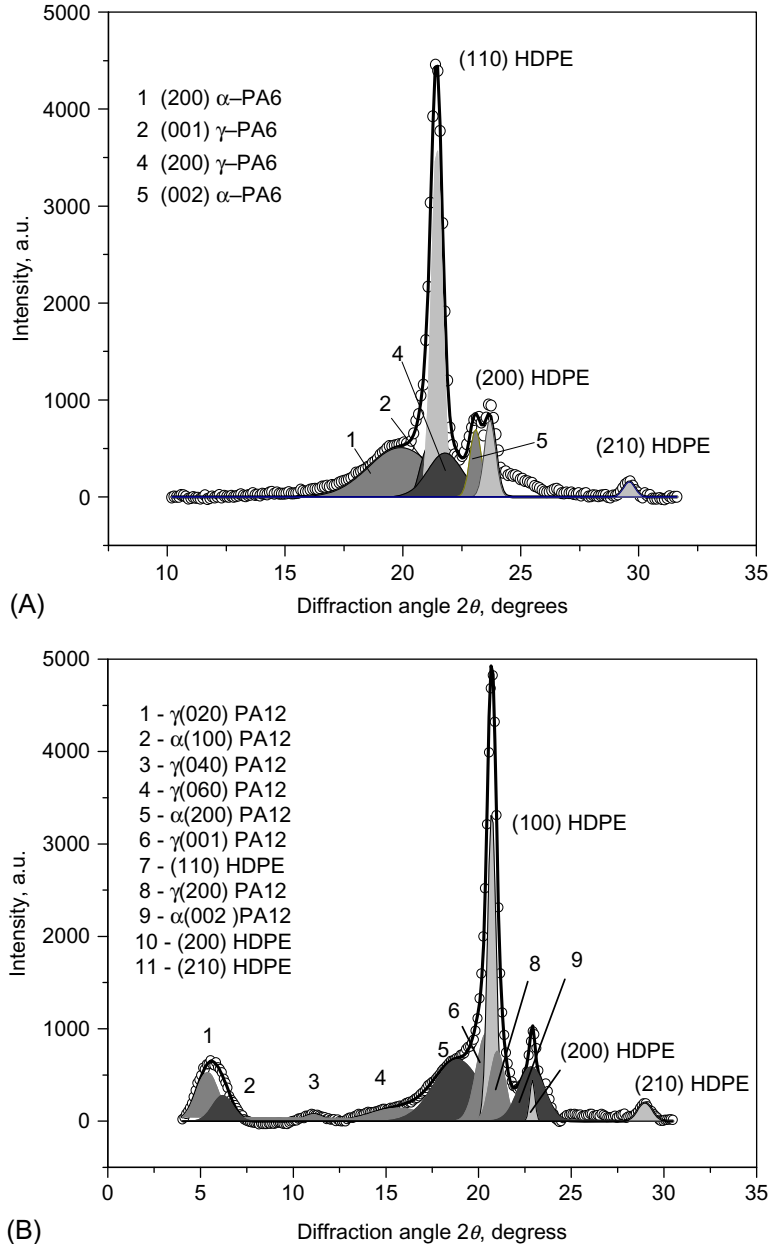

Fig. 7.12 Example of peak fitting for typical MFC samples after separation of the total WAXS: (A) $\Phi_{aniso}(s)$ of HDPE/PA6/YP = 80/20/0; (B) $\Phi_{aniso}(s)$ of HDPE/PA12/YP = 80/20/0;

Continued

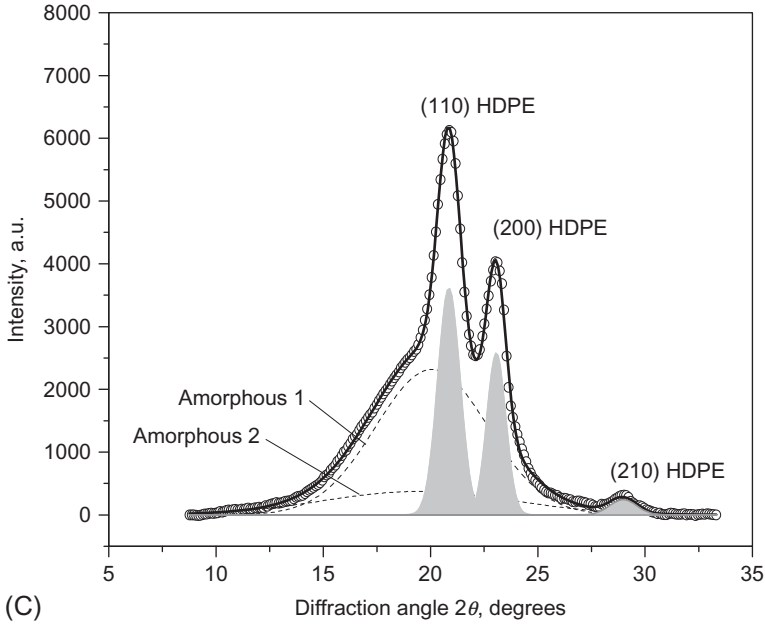

Fig. 7.12, cont'd (C) $\Phi_{iso}(s)$ typical for all MFC irrespective of the polyamide reinforcement. Modified from Dencheva N, Stribeck A, Denchev Z, Nanostructure development in multicomponent polymer systems and its characterization by X-ray scattering. Eur Polym J 2016;81:447–469.

Table 7.3 displays the data extracted from the fitted WAXS patterns for the MFC without and with compatibilizer, i.e., HDPE/PA6/YP = 80/20/0 and 70/20/10. The percentage of WAXS produced by the oriented content of the PA6 fibrils and that of the oriented, transcrystalline HDPE is 1.03:1.00 in the compatibilized MFC and 1.26:1.00 in the noncompatibilized MFC. This means that in the presence of compatibilizer a larger part of the HDPE is included into the TCL without changing considerably its crystallographic characteristics. Based on the *d*-spacing values it can be concluded that the HDPE unit cell is slightly larger in the bulk matrix, as compared to that in the oriented TCL.

Based on the peak-fitted oriented WAXS, results analogical to those in Table 7.3 can be obtained for all MFC studied. The relationship $f = \Phi^{PA}_{aniso}(s)/\Phi^{HDPE}_{aniso}(s)$ can be calculated in each case and can be further used to obtain an estimate of the TCL thickness in uniaxially oriented MFC materials. Such estimation is based on the following theoretical considerations.

In the first place, the analysis of the data in Table 7.3 based on the simple pseudo-isotropized contribution $\Phi_{aniso}(s)$ and its comparison to the analysis of $\Phi_{iso}(s)$ demonstrated that in the bulk isotropic fraction only HDPE is crystallized and crystallized PA6 is only found in the anisotropic fraction. Moreover, there is also anisotropically crystallized HDPE. This finding supports the morphological model sketched in

Table 7.3 Deconvolution of the oriented and isotropic WAXS for two HDPE/PA6/YP MFC

WAXS reflections	HDPE/PA6/YP					
	80/20/0			70/20/10		
	2θ, (degrees)	Content, (%)	d_{hkl}, (Å)	2θ, (degrees)	Content, (%)	d_{hkl}, (Å)
Oriented part of WAXS intensity $\Phi_{aniso}(s)$						
(200)—α PA6	19.90	28.5	4.34	19.92	28.7	4.34
(001)—γ PA6	21.05	6.6	4.11	21.35	7.6	4.07
(110)—HDPE	21.44	34.9	4.03	21.33	38.2	4.05
(200)—γ PA6	21.79	13.7	3.97	21.66	7.6	3.99
(002)/(202)—α PA6	23.09	6.9	3.75	22.99	6.9	3.76
(200)—HDPE	23.69	7.9	3.65	23.74	9.1	3.65
(210)—HDPE	29.61	1.5	2.94	29.50	1.9	2.95
PA6 fraction, (%)		55.7			50.8	
HDPE fraction, (%)		44.3			49.2	
f = PA6/HDPE		1.26			1.03	
Isotropic part of WAXS intensity $\Phi_{iso}(s)$						
(110)—HDPE	21.13	14.6	4.09	20.97	9.8	4.12
(200)—HDPE	23.56	11.4	3.67	23.48	12.6	3.69
(210)—HDPE	29.29	1.9	2.96	29.24	1.3	2.97

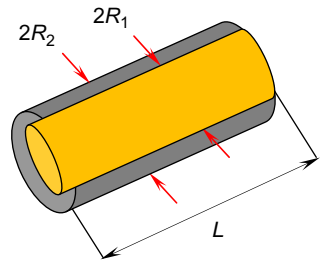

Fig. 7.13 Model of a shell-core polyamide fibril covered by transcrystalline HDPE.

Fig. 7.13, and a quantitative determination of the dimensions of PA core and HDPE shell is of interest. Second, from theoretical point of view, splitting of $\Phi_{\text{aniso}}(s)$ from MFC into components from PA and PE is surely possible qualitatively. For the quantitative TCL thickness estimation one needs to separate into components the *total crystalline intensity* irradiated into the complete reciprocal space. Since the information contained in the measured WAXS patterns in Fig. 7.12 does not cover the complete reciprocal space, the TCL thickness can be assessed only approximately. Two

simplifying assumptions should be thereby applied: (i) the contributions of the meridional reflections of PA and HDPE can be neglected because of their weakness and (ii) mapping of the WAXS fiber data from the surface of Ewald's sphere to the (s_{12},s_3) plane may be omitted. Then, the approximately isotropized total anisotropic component of the WAXS intensity is:

$$\widetilde{I}_{\text{tot,ani}}(\text{s}) = 2\pi s \int_0^{\pi} \Phi_{\text{aniso}}(s,\chi)\, \sin\chi\, d\chi \tag{7.3}$$

with $\chi = 0$ defining the fiber axis and $2\pi s_{12} = 2\pi s \sin\chi$ being the the circumference of the circle in reciprocal space. The corresponding total isotropic component of the WAXS is well-known, does not require approximation, and reads:

$$I_{\text{tot,iso}}(s) = 4\pi \text{s}^2 \Phi_{\text{iso}}(s) \tag{7.4}$$

The curves according to Eqs. (7.3), (7.4) can be deconvoluted by peak-fitting, as has been done with the pseudo-isotropized curves. Summarizing, in order to compute the relative thickness of the oriented TCL, we resort to the result of Ruland [48], that the scattering intensity of a crystalline component $I_{\text{tot},c}$ integrated over the whole reciprocal space is proportional to the number of electrons $N_{\text{el},c}/V$ which belong to this phase, V being the irradiated volume. This means in our notation

$$N_{\text{el},c}/V \propto \int_0^{\infty} I_{\text{tot},c}(s)\, ds \tag{7.5}$$

and the proportionality factor is a geometric factor which is the same for all components in the material. In other words, after applying the above approximations and simplifying assumptions, the accessible scattering intensities of the oriented transcrystalline HDPE and oriented polyamide will be proportional to their volume.

For the particular MFC samples in this study, the volume fractions of the components in the TCL are readily established after computation of the electron densities $\rho_{\text{el,PE}}$ and $\rho_{\text{el,PA}}$ of the amorphous and of the crystalline phases of PE and PA, respectively [49]:

$$\rho_{\text{el},\,i} = N_A \frac{Z_M}{M_M} \rho_m \quad \left(\text{electron units/nm}^3\right) \tag{7.6}$$

with ρ_m, being the respective average mass density, N_A the Avogadro's number (6.022×10^{23} mol^{-1}), Z_M the number of electrons per monomer unit and M_M—the molecular weight of molecule or monomer unit.

If we denote by V_{PA} the volume of the PA core, in agreement with the model in Fig. 7.5, it can be written that

$$V_{\text{PA}} = \pi L R_1^2 \tag{7.7}$$

and

$$V_{\mathrm{TCL}} = \pi L\left(R_2^2 - R_1^2\right) \tag{7.8}$$

Combining Equation 10 with 11 and 12, the following simple dependence can be deduced between the visible by SEM fibril radius R_2 and that of the PA core R_1:

$$R_1^2 = R_2^2 \cdot \sqrt{\frac{f}{k+f}} \tag{7.9}$$

wherein $k = \rho_{\mathrm{PA}}/\rho_{\mathrm{HDPE}}$ and $f = \Phi_{\mathrm{aniso}}^{\mathrm{PA}}(s)/\Phi_{\mathrm{aniso}}^{\mathrm{HDPE}}(s)$.

Table 7.4 summarizes the structural information related to the reinforcing fibrils as revealed by the SEM and WAXS methods (i.e., $2R_1$, $2R_2$ and R_2–R_1) for MFC materials without MMT reinforced by either PA6 or PA12. The $2R_2$ values were obtained by averaging of 3–5 fibril thicknesses per sample as measured during the SEM observation. The same table contains also the respective data for the Young's modulus E, ultimate stress $\sigma_{\max}$, and flexural stiffness C_R, of the respective MFC as well as of the neat HDPE matrix and the neat oriented polyamides. It can be concluded that the formation of TCL is a common feature for all MFCs containing either PA6 or PA12. There can be a significant difference between the TCL thicknesses in PA6 and PA12 reinforced composites, as well as in the compatibilized and noncompatibilized MFCs with the same reinforcement. Compatibilization results in thinner fibrils in which not only the polyamide core, but also the TCL are finer. In the PA6 reinforced MFC the TCL is notably thicker than in the PA12-containing system. Judging from Table 7.4, the TCL thickness can be related to the mechanical performance of the MFCs. No matter that the longitudinal E value of neat oriented PA6 is much higher than that of oriented PA12, the respective compatibilized and noncompatibilized MFC

Table 7.4 Dependence between the morphological parameters of the fibrils (R_2, R_1, and TCL) calculated from WAXS or determined form SEM data and the mechanical behavior in various MFC [44]

	HDPE/PA6/YP		HDPE/PA12/YP				
	80/20/0	70/20/10	80/20/0	70/20/10	PA6	PA12	HDPE
$2R_2$, (nm)	750	500	625	560			
$2R_1$, (nm)	550	350	535	453			
TCL = R_2–R_1	100	75	45	54			
E, (MPa)	1095	920	1054	972	3180	2240	827
σ_y, (MPa)	57	37	64	55	230	233	26
C_R, (MPa)	2624	2294	3414	3404	–	–	1478

Notes: E is the longitudinal secant modulus determined at 1% strain; $\sigma_{\max}$, is the maximum stress at break and C_R is the three point support flexural stiffness determined according to Nunes et al. [40].

display similar moduli. At the same time, the σ_{max} of the HDPE/PA12/YP materials are significantly higher. It is to be noted the superior flexural stiffness of the PA12-reinforced MFC. This can be attributed to the lesser TCL thickness and the better orientation of the PA12 fibrils achieved in the stage of cold drawing.

7.2.3.4 Simultaneous straining/small angle X-ray scattering

The research in the previous subsection was based on the fact that in static conditions (i.e., without changing the sample's dimension, temperature or other parameter during the test), electron microscopy and X-ray scattering are useful complements to each other. Unfortunately, SEM and TEM techniques require quite complex sample preparation making impossible to follow the structure evolution in dynamic conditions, e.g., under cyclic or continuous strain. At the same time, the biggest limitation of the X-ray techniques is that they produce information in the reciprocal space that may require relatively complex data processing to extract the structural information. Our recent works on the structural characterization of HDPE/PA MFC systems showed undoubtedly the large potential of the simultaneous synchrotron SAXS/straining experiments in both HDPE/PA/YP oriented precursors and unidirectional MFC on their basis. They consist in obtaining simultaneously, with one and the same sample, of two data sets: (i) stress-strain curve from a tensile testing machine incorporated into a synchrotron beamline, and (ii) nanostructural changes within the sample from a number of two-dimensional synchrotron SAXS patterns taken during the straining experiment. The SAXS and tensile output data were collected and processed by a semiautomatic method based on the computation and interpretation of the evolution of the multidimensional chord distribution function (CDF) [50].

The details concerning the CDF data accumulation, treatment, and interpretation in HDPE/PA precursors and MFC will not be presented here since they fall out of the scope of this chapter. The reader is encouraged to consult the previously published works on these subjects [51–53]. In general, this innovative approach allows relating the macrodeformation of the test sample to the evolution of the nanodeformation within this sample, the latter being characterized by the changes in the respective crystalline domain dimensions as expressed by their long period L.

Fig. 7.14 presents the quantification of the tensile properties and the nanostructural changes in the samples with compositions HDPE/PA6/YP = 80/20/0 and 70/20/10 as a function of the true stress σ and the true elongation ε_m. In both graphs the abscissa indicates the time from the beginning of the straining, and the ordinate—the evolution of six parameters (two mechanical and four structural) during the experiment, each of them being in its respective dimension. The structural parameters are: the long period values related to the peaks of transcrystalline HDPE (meridional L_m^{HDPE} and equatorial L_{eq}^{HDPE}), to the PA6 reinforcing fibrils (meridional L_m^{PA6}), and the lateral extension e_l of the HDPE domains from TCL. These parameters were computed from the respective negative faces of the CDF during the straining experiment applying an automatic procedure [51].

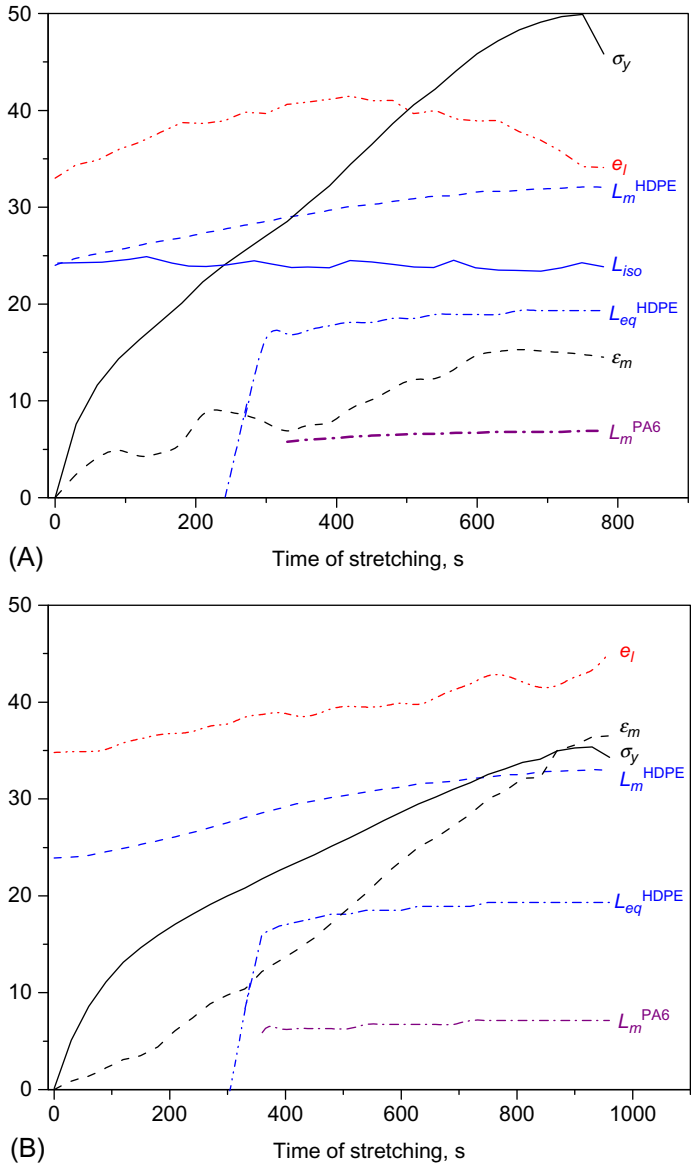

Fig. 7.14 Evolution of the nanostructural parameters during the simultaneous SAXS/straining of HDPE/PA unidirectional MFC: (A) HDPE/PA6/YP = 80/20/0; (B) HDPE/PA6/YP = 70/20/10. All nanostructural data are obtained from the respective negative face CDF peaks computed on the basis of azimuthally dependent $\Phi_{aniso}(s,\chi)$. Legend: longitudinal stress σ_y (MPa); macroscopic strain ε_m (%); meridional long period of transcrystalline HDPE domains L_m^{HDPE} (nm); equatorial long period L_{eq}^{HDPE} (nm) of strain-crystallized HDPE; meridional long period L_m^{PA6} (nm) of PA6; lateral extension e_l (nm) of the meridional transcrystalline HDPE domains.

Modified from Dencheva N, Stribeck A, Denchev Z, Nanostructure development in multicomponent polymer systems and its characterization by X-ray scattering. Eur Polym J 2016;81:447–469.

The stress at break σ_b and the macroscopic strain at break ε_{mb} of the two samples show that the noncompatibilized MFC (Fig. 7.14A) is less ductile than the one with 10% YP (Fig. 7.14B), showing ε_{mb} values of 15% and 36%, respectively. At the same time, the $\sigma_b = 50$ MPa in the noncompatibilized sample is significantly higher than that of the YP-containing sample being slightly above 30 MPa. These stresses and strains at break are in good agreement with previously discussed mechanical data of these MFC obtained in a commercial testing machine under slightly different conditions (Figs. 7.5 and 7.6 and Table 7.4).

Despite their different mechanical behavior, the two MFC in Fig. 7.14 display similar structural developments under continuous strain. The starting L_m^{HDPE} values in both MFCs are in the range of 22–23 nm and gradually grow to 32 nm just before sample failure. Notably, there is no such growth in the long periods related to the isotropic matrix HDPE (L_{iso}, shown only in Fig. 7.14A). The starting L_{iso} values in both composites are identical to L_m^{HDPE} and at the end of the straining experiment even drop with 1–2 nm. The long periods of the reinforcing fibrils L_m^{PA6} vary very slightly between 6 and 7 nm, being independent of the compatibilizer content. The equatorial long spacing L_{eq}^{HDPE} in the two MFCs related to the strain-induced crystallization of HDPE domains from the matrix, appears abruptly at about 7%–8% of strain with values of 16–17 nm, increasing to 19–20 nm close to sample failure. The presence of compatibilizer YP causes some structural differences. In the noncompatibilized 80/20/0 MFC the lateral extension e_l of the HDPE domains from TCL before strain is 33 nm, passes through a maximum of 41.5 nm at ε_m close to 10% and then decreases reaching just before break its initial values. Instead, in the 70/20/10 MFC e_l monotonously grows from 35 to 45 nm.

The images in Fig. 7.15 show the both CDF faces of two MFC sample before and after mechanical failure. Interestingly, the equatorial long spacing for the second HDPE domain in TCL with L between 17 and 30 nm disappears (cf. the images in columns 1 and 2). Hence, the suggested strain induced crystallization is a reversible

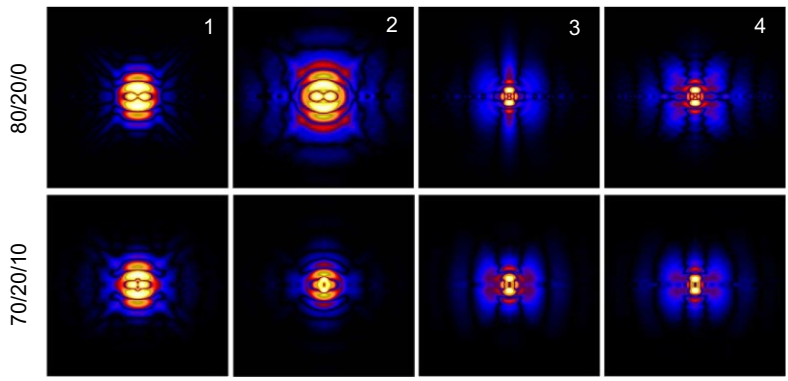

Fig. 7.15 Comparison between the CDF for MFC based on HDPE/PA6 without and with compatibilization before strain and after sample failure and relaxation: 1, MFC before strain at 30°C; 2, MFC after mechanical failure at 30°C; 3, MFC before strain at 160°C; 4, MFC after strain and relaxation at 160°C. Fiber axis and strain direction are vertical [53].

process for the MFC materials without MMT. Moreover, analyzing the CDF shapes and positions, an axial growth of the transcrystalline HDPE domains from 23–24 to 27 nm is observed due to the extreme mechanical load. In the uncompatibilized 80/20/0 MFC the perfection of the transcrystalline HDPE domain orientation is decreased, which is evidenced by the change of shape of the CDF peaks. In this sample the loss of correlation among the domains in straining direction is low. In the HDPE nanostructure of the compatibilized 70/20/10 MFC the extreme mechanical load causes mainly a relative decrease of the lateral extension of the domains, i.e., a transition from lamella to grain.

The changes in the PA6-nanostructure can be studied from the CDF patterns at 160°C (Fig. 7.15, columns 3 and 4). Under these temperature conditions the HDPE is molten. The uncompatibilized MFC before straining (col. 3) shows highly ordered PA6 microfibrils almost uncorrelated in lateral direction, which after sample failure (col. 4) gain such correlation. The off-meridional streaks have moved after failure closer to the meridian, there is even a second order of off-meridional streaks. This indicates the beginning of 3D macrolattice formation. In the compatibilized material such macrolattice inside the PA6 microfibrils exists even before straining, and the ultimate strain results in a slight decrease of its correlation.

Combining the information from Figs. 7.14 and 7.15, a model of the scattering ensembles existing in the MFC at various stages of the straining can be suggested. The cartoon in Fig. 7.16 visualizes the reversible strain-induced crystallization of matrix material in the presence of the oriented transcrystalline HDPE shell of the PA6 reinforcing fibrils.

Fig. 7.16A depicts three transcrystalline HDPE domains on the PA6 fibril surface correlated along the sample meridian. Before straining, the lamellae tip domain is in contact with amorphous HDPE matrix material containing macromolecules with varying degree of entanglements. At low strains ($\varepsilon_m < 7\%–10\%$) the tip TCL domain grows in lateral direction involving some less entangled HDPE macromolecules that are able to crystallize (Fig. 7.16B, the arrow-indicated process). As seen in Fig. 7.14B, the lateral lamellae extension e_l in the YP-containing MFC is constant with the strain

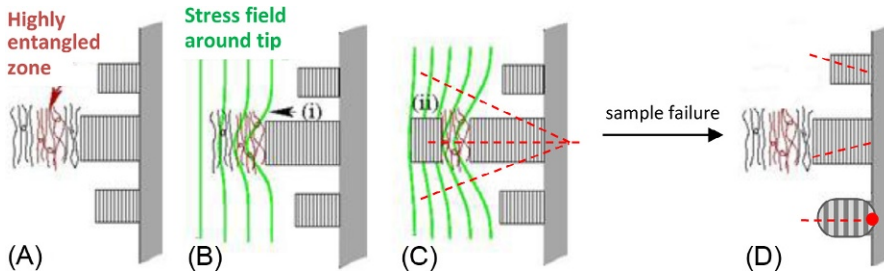

Fig. 7.16 Schematic presentation of the stress-induced crystallization of HDPE matrix material during the continuous strain of HPDE/PA6 microfibrillar composite: (A) at $\varepsilon_m = 0$; (B) at $\varepsilon_m < 7\%–10\%$; (C) at $\varepsilon_m > 7\%–10\%$; (D) after sample failure. (i), tip HDPE domain and the direction of its growth; (ii), strain-crystallized (satellite) HDPE domain [53].

increase until sample failure, while in MFC without compatibilization (Fig. 7.14A) it passes through a maximum. In agreement with the "minimum crystallization distance" concept of Strobl, the highly entangled zone cannot be entered by any other crystalline lamella growing during the strain-induced crystallization [54]. Hence, the process is transferred to the next crystallizable area. Above a certain density of the stress field (at $\varepsilon_m > 7\%$ for the 80/20/0 sample and above 10% for the 70/20/10 one), a new (called also "satellite") HDPE crystalline domain appears (Fig. 7.16C, *ii*), its far end being quite well defined with respect to the tip domain. For both MFC in the beginning of the straining the tip and the satellite domains are positioned in front of each other, i.e., normally to the straining direction. As the strain increases, this perfect frontal alignment becomes distorted and the satellite domain may be repositioned slightly above or below the tip domain as depicted by the dashed lines in Fig. 7.16C. After sample failure (Fig. 7.16D), the satellite domains melt and the axial correlation of three HDPE domains is preserved in both MFC. In the noncompatibilized MFC some loss of their axial alignment (i.e., different inclinations in respect to the normal to the straining direction) may be deduced. In the compatibilized MFC, where the TCL domains are chemically bonded to the PA6 fibril (the dot in Fig. 7.16C), their lamellar geometry transits into grains as schematically indicated in the same figure.

This last study allows relating the differences in the mechanical performance of the compatibilized and noncompatibilized MFC containing 20 wt% of YP with their fine crystalline nanostructure assessing information which is impossible to reveal by other analytical methods.

7.3 Dually reinforced polyethylene-polyamide MFC

As verified by the mechanical data of HDPE/PA-based MFC discussed for far, the improvement in their final mechanical properties that has to be related to the polyamide microfibrillar reinforcement is limited by the stiffness, strength, and flexibility of the latter. It was also demonstrated that changing the polyamide type, i.e., from PA6 to PA12, could create additional possibilities for control and improvement. An alternative to this approach is to try to additionally strengthen the PA6 fibrils by introducing into them mineral or organic fillers. The use of various nanostructured organically treated MMT nanoclays (o-MMT) in HDPE/PA6 based MFC was explored by us in a series of studies [51–53] and in a doctoral thesis [55]. Very recently, the dual reinforcement of HDPE by polyamide microfibrils and MMT was revisited by other authors [56,57]. Interesting possibilities for additional reinforcement of these systems by wood flour or other natural fibers were investigated in earlier publications [58,59]. In the next subsection the use of MMT nanoclays in HDPE/PA6-based systems will be reviewed since these studies possess the most systematic character.

7.3.1 Initial studies on PA6/MMT hybrid composites

The main point of these studies was relating the structure and composition of the microfibril forming component of MFC (in this case that will be a PA6/MMT hybrid nanocomposite) to its mechanical properties. This hybrid was prepared by melt

compounding involving various amounts of different MMT-based organically modified nanoclays. Prior to any further processing, the pelletized neat PA6, the masterbatch of PA6 with 20 wt% of predispersed/exfoliated organophilic Nanomer I.24 TL (designated as MB20NM) and the Cloisite 15A clay were dried for 10 h at 90° C under slight vacuum. Then the commercial MB20NM was diluted with the respective amounts of neat PA6 to systems containing 1.0–7.5 wt% of MMT by melt blending in a Leistritz counter-rotating twin-screw laboratory extruder with a medium to high shear configuration. The temperature was set to 245°C in all the seven heating zones. The extruder was coupled to a cooling bath and a pelletizer equipped with air drier. Similar extruder configuration and conditions were used to produce PA6/clay masterbatch containing 10 wt% of Cloisite 15A (MB10CL). MB10CL was consequently diluted to 4 and 5 wt% with neat PA6. The composition of all PA6/clay composites is shown in Table 7.5. The pelletized PA6/MMT hybrid composites with different amounts of Nanomer (NM) or Cloisite (CL) were dried and compression-molded into plates with a thickness of 1.0 mm in a hot press with a pressure of about 10 MPa at 250°C. Plates from the neat PA6, the MB20N and MB10CL compositions were also produced under the same conditions. These plates were used to produce test samples for the tensile tests. All the details of the preparation can be found elsewhere [55].

Table 7.6 shows the tensile behavior of the PA6 hybrids as a function of the o-MMT amount and type comparing it to the matrix PA6. It allows the conclusion that the hybrids with 2.5% and 5.0% NM seem to show the best set of tensile properties: an improvement in respect to the matrix of 22% and 15% for σ_y and 27% and 62% for the Young's modulus. The latter can be enhanced further with higher loads of clay but in detriment of the ultimate tensile stress. In the hybrid containing 5% CL, the respective improvements for E and σ_y were slightly lower as compared to the 5% NM sample.

To explain the differences in the mechanical properties of PA6 hybrids with different MMT reinforcements, synchrotron WAXS studies were performed. The long spacing of the (001) basal reflection $d_{(001)}$ of the layered clay is related to the height of the galleries between the inorganic sheets [60]. The increase of $d_{(001)}$ of MMT in the

Table 7.5 Compositions of the studied PA6/nanoclay hybrids

Raw materials	Organically treated MMT	Clay content, (wt%)	Sample designation
PA6, MB20NM	–	1.0	1 NM
	–	2.5	2.5 NM
	–	4.0	4 NM
	–	5.0	5 NM
	–	7.5	7 NM
PA6	CL 15 A	10.0	MB10CL
PA6, MB10CL	–	4.0	4 CL
	–	5.0	5 CL

Table 7.6 Mechanical properties of PA6/MMT nanocomposites extracted from the stress-strain curves

Sample	Young's modulus E, (MPa)	$\triangle E$, (%)	Tensile strength σ_{max}, (MPa)	$\Delta\sigma_{max}$	Elongation at break ε, (%)
PA6	1350 ± 17	0.0	59.3 ± 1.3	0.0	162.0
1% NM	1640 ± 23	21.5	66.8 ± 2.2	12.6	15.0
2.5% NM	1710 ± 41	26.7	72.1 ± 2.8	21.63	14.4
5% NM	2180 ± 19	61.5	68.1 ± 3.1	14.9	4.0
7.5% NM	2300 ± 22	70.4	59.9 ± 2.8	1.0	1.1
5% CL	2001 ± 62	48.2	64.9 ± 2.8	9.6	9.7
MB20NM	2870 ± 43	112.6	18.9 ± 1.0	−68.1	0.2
MB10CL	2230 ± 57	65.2	16.7 ± 1.0	−71.8	1.1

Note: The MB20NM commercial masterbatch available from Nanocor Inc. contains 20 wt% of Nanomer I24 TL clay. CL = Cloisite 15A clay originating from MB10CL; NM = Nanomer I24 TL clay originating from MB20NM. Modified from Motovilin M. Development and investigation of new hybrid composite materials based on oriented blends of thermoplastic polymers and nanosized inorganic fillers [Ph.D. thesis]. University of Minho; 2011. https://repositorium.sdum.uminho.pt/bitstream/1822/14250/1/Thesis_Mladen%20Motovilin_2011.pdf.

presence of the matrix polymer can be associated to the various degrees of clay delamination denoted as intercalation and exfoliation.

By means of synchrotron WAXS and SAXS, Motovilin et al. [61] revealed how mixing of different o-MMT brands affects the nanostructure of both nanoclay and matrix and how these structural effects change the mechanical properties. Thus, Fig. 7.17 compares the WAXS patterns of the two o-MMT sources used in this work—NM I.24 TL and CL15A at 30°C. It can be seen that there exist small but clear differences between these two materials. The d_{001} values of the organically treated CL and NM obtained from the (001) reflections of the organically modified samples correspond to expanded gallery heights of c.29 and 20 Å, respectively. Some amounts of Na-MMT are also observable in both MMT samples (being larger in CL), with 001 reflections corresponding to 12.4 and 10.0 Å. Higher order MMT reflections were also identified in both samples in Fig. 7.17. The strongest ones are those of the 020 and 006 crystalline planes, as well as of a specific crystalline phase called Opal Cristobalite CT [62]. The angular position, shape, and intensity of the MMT peaks were found to be independent on the heat treatment.

Fig. 7.18 visualizes the way deconvolution and fitting of the WAXS patterns was performed for all PA6-MMT nanocomposites, exemplifying it for the PA6 hot-pressed plate containing 7.5% NM at 30°C. The inset shows the range of the 001 reflection with its peak at $s = 0.222\ nm^{-1}$ corresponding to a d-spacing of 46 Å. Decreasing the MMT amount, this value goes up to 48–50 Å, thus reaching the limit of resolution of the WAXS setup used. This leads to the conclusion that the absence of a (001) basal peak of MMT may not necessarily mean complete exfoliation with distances between the silicate sheets of several nanometers and more. Nevertheless, in

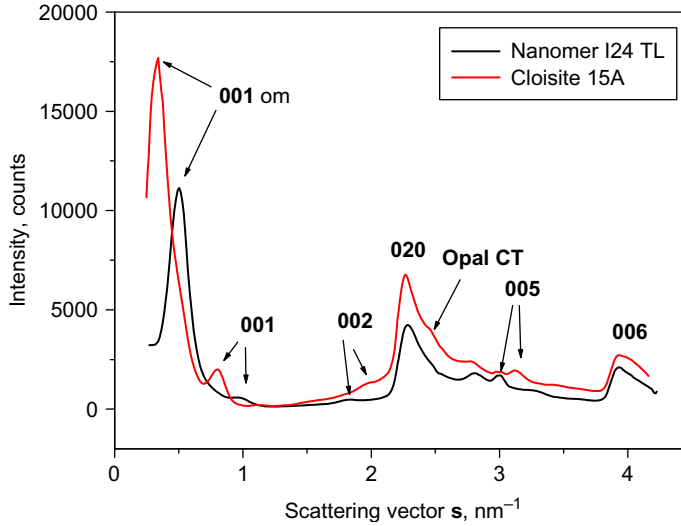

Fig. 7.17 WAXS patterns of the two montmorillonite brands at 30°C. om = organically modified; Opal CT = opal cristobalite.
Modified from Motovilin M, Denchev Z, Dencheva N. On the structure-properties relationship in montmorillonite-filled polyamide 6 nanocomposites. J Appl Polym Sci 2011;120:3304–3315.

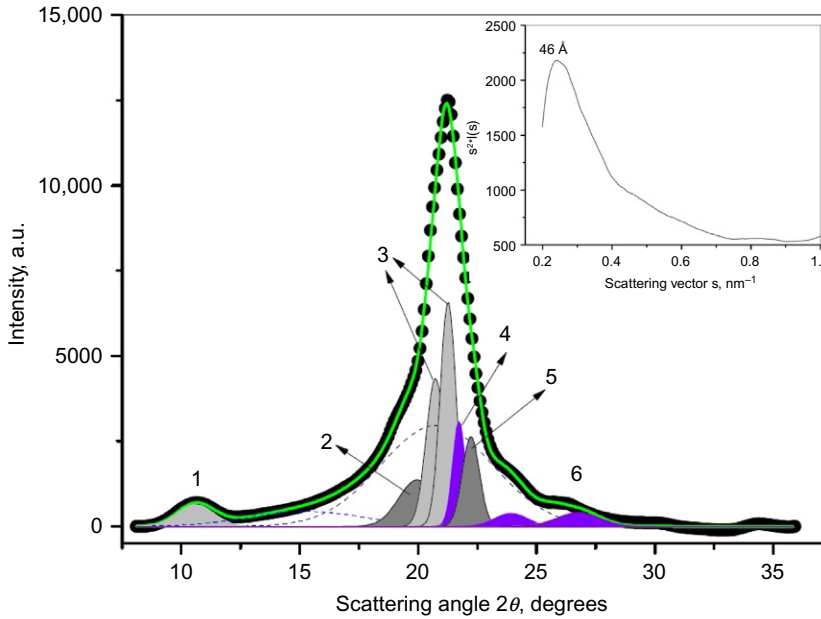

Fig. 7.18 Example of fitting the WAXS patterns of PA6 hot-pressed plate containing 7.5% NM: 1, (020) reflection of γ-PA6; 2, (200) and (002/202) reflection of the α-PA6; 3, (200) reflection of the γ-PA6; 4, Opal CT reflection of NM; 5, weaker reflections of the NM phase. The two broad Gaussian peaks represent the contribution of the diffuse scattering (amorphous halo).The inset shows the WAXS curve in the 0.1–1.0 nm^{-1} range of the scattering vectors [61].

the presence of PA6 the galleries height of the o-MMT expands almost twice due to the effective intercalation of the polyamide macromolecules.

A monoclinic unit cell lattice was assumed for the α-PA6 form with two peaks corresponding to α(200) and α(002/202) crystalline planes (Fig. 7.18, the peaks denoted with 2). For the γ-crystalline form, pseudo-hexagonal unit cell was supposed, with one Gaussian for the γ(001) reflection (peak 1) and two almost coinciding Gaussians for the γ(200) crystalline plane with 2θ between 21 and 22 degrees (peak 3). From the MMT peaks in Fig. 7.4, the Opal CT peak close to 22 degrees was used in the fitting (peak 4), as well as the series of weaker crystalline peaks in the angular range between 24 and 34 degrees. On the basis of these fits, the crystallinity indices X_c and the relation α/γ was calculated for all nanocomposites samples as a function of the MMT type and concentration (Table 7.7). Apparently, with the increase of the Nanomer amount, the X_c of the matrix gradually decreases. Moreover, the samples with 2.5% and 5.0% of Nanomer were richer in α-PA6 polymorph while the sample with 7.5% NM and the NM masterbatch displayed significantly larger amounts of the γ-PA6. Comparing the composites with 5% of NM and 5% of CL shows that the latter nanoclay enhances stronger the formation of the γ-PA6 polymorph in the matrix. The same trend is revealed also in the two masterbatches MB20NM and MB10CL.

The direct observation of PA6/MMT hybrids by TEM and FT-IR microscopy allowed the conclusion that exfoliated nanostructure was only obtained in the case of 1% NM. In the rest of the samples tactoids with various dimensions were always observable. The SAXS data and their treatment with the linear correlation function formalism showed that the MMT clay enhances the formation in the PA6 matrix of larger periodicities (lamellar stacks) with long spacings growing from 90 to c.120 Å due to expansion of both crystalline and amorphous layers [61].

7.3.2 Structure-properties relationship in HDPE/PA MFC with clay

The MFC samples based on HDPE and PA6 reinforced by various amounts and types of MMT were obtained in the same way as the respective systems without nanoclay. First the oriented precursors were prepared in the extruder line in Fig. 7.4. The

Table 7.7 Crystallinity data obtained from the fittings of the WAXS patterns of PA6/MMT nanocomposites

Sample	WAXS X_c (%)	α-content (%)	γ-content (%)	α/γ
PA6	45.1	28.5	16.6	1.71
2.5% NM	39.6	35.4	4.2	8.44
5% NM	38.0	22.2	15.8	1.40
7.5% NM	35.9	8.0	27.9	0.29
5% CL	38.9	11.5	27.4	0.42
MB20NM	33.8	10.5	23.2	0.45
MB10CL	43.7	10.6	33.1	0.32

For sample designation see Table 7.5.

PA6/nanoclay pelletized component was premixed with the respective amounts of HDPE and YP granulates, and fed to the extruder working at the conditions indicated in Table 7.8. After the extrusion blending and fibrillation stage, at the exit of the last haul-off unit the HDPE/PA-MMT/YP blends were obtained in the form of continuous OC or MRB. NOG of each blend were also obtained by pelletizing the extrudate directly after the cooling bath. Each precursor composition was obtained in two different ways: with melt preblending of MB20NM and MB10CL with neat PA6 or without such preblending. In the first case, the desired concentration of MMT in the PA6

Table 7.8 Designation of the HDPE/PA6/YP = 80/20/0 and 77.5/20/2.5 samples specifying the amount and type of the MMT, as well as the way of preparation

Wt% in MFC			MMT wt% in PA6			
HDPE	**PA6**	**YP**	**NM**	**CL**	**Preblending**	**Sample designation**
80	20	0	1	–	+	1 NM 820
77.5	20	2.5	1	–	+	1 NM 722
80	20	0	2.5	–	+	2.5 NM 82
77.5	20	2.5	2.5	–	+	NM 722
80	20	0	4	4	+	4 NM 82 4 CL 82
80	20	0	4	4	–	4 NM 82 IS 4 CL 82 IS
77.5	20	2.5	4	4	+	4 NM 722 4 CL 722
77.5	20	2.5	4	4	–	4 NM 722 IS 4 CL 722 IS
80	20	0	5	5	+	5 NM 82 5 CL 82
80	20	0	5	5	–	5 NM 82 IS 5 CL 82 IS
77.5	20	2.5	5	5	+	5 NM 722 5 CL 722
77.5	20	2.5	5	5	–	5 NM 722 IS 5 CL 722 IS
80	20	0	7.5	–	+	7.5 NM 82
77.5	20	2.5	7.5	–	+	7.5 722
Extrusion temperature of precursors: 250°C						
Compression molding of composites: 160°C						
Composite types: UDP, CPC, MRM, NOM						

NM = Nanomer originating from MB20NM; CL = Cloisite 15A originating from MB10CL; YP = Yparex.
Modified from Motovilin M. Development and investigation of new hybrid composite materials based on oriented blends of thermoplastic polymers and nanosized inorganic fillers [Ph.D. thesis], University of Minho; 2011, https://repositorium.sdum.uminho.pt/bitstream/1822/14250/1/Thesis_Mladen%20Motovilin_2011.pdf.

component was achieved by diluting each of the masterbatches with neat PA6. Then, in an additional separate extrusion, the resulting PA6/MMT granules were melt-blended with the respective amounts of HDPE and YP to get after cold-drawing and cutting the respective OC or MRB. In the case without preblending, weighed amounts of each masterbatch, of neat PA6 and of YP were melt-mixed in the extruder directly (i.e., in situ) and cold-drawn to oriented precursors. The in situ obtained compositions received the index "IS" in Table 7.8.

The differently aligned arrays of precursors with various compositions were subjected to selective isotropization by compression molding at 160°C and 10 MPa thus producing UDP, MRM, and NOM plates with thickness of 1.0–1.4 mm. For flexural and impact tests CPC plates were obtained by crossing bundles of mutually perpendicular oriented cables that were studied with the MRM and NOM plates [55].

7.3.2.1 Mechanical properties

All composite materials were studied in tension, flexion, and impact applying the same method described in Section 7.2.3.1. As seen in Table 7.9, the longitudinal tensile Young's modulus E and maximum stress σ_{max} of the clay-containing UDP laminae are always better than the HDPE matrix. However, the feasibility of these UDP with dual reinforcement will determined by the comparison to those without nanoclay. Thus, as regards the E values, most all MMT-containing UDP perform better, whereby the higher the MMT content, the higher the modulus, the best values being around 1200 MPa. In the presence of 2.5% YP, this trend is preserved. In all samples of Table 7.9 premixing of PA6 and MMT masterbatch in the sage of sample preparation leads to higher E-values as compared to the in situ samples (IS). The high stiffness of the dually reinforced noncompatibilized UDP comes with some detriment of the σ_{max}, its values reaching 53 MPa in the 5 CL 82 sample, while the UDP without clay showed 57 MPa. In the presence of YP the maximum stress values grow to 59 MPa in the 5 NM 722 sample representing a 30% improvement in respect to the 77.5/20/2.5 reference without clay. It can be therefore concluded that the dual reinforcement of the UDP with PA6 and MMT is beneficial in all samples as far as the longitudinal stiffness E is concerned. Compatibilization with YP allows the combination of high E and σ_{max} in UDP whose fibrils contain 4%–5% NM or CL introduced by preblending. It should be noted that stiffness and strength in transversal direction, i.e., normally to the fibrils' axis are significantly lower, and are close to or even lower than the values of the matrix HDPE.

Fig. 7.19 compares the longitudinal E values of UDP and MRM composites containing various amounts and types of nanoclay. It can be seen that the isotropic MRM samples without YP display E-values in the range of 1 GPa that, on compatibilization, grow with 10% being always higher than those of the respective MRM without nanoclay varying around 0.9 GPa. The σ_{max} values of the MRM (not shown in Fig. 7.19) are in the range of 30–40 MPa, i.e., better than the HDPE matrix and significantly higher than in MRM materials without clay that are in the range of 22–24 MPa, however far below the respective longitudinal values of the UDP materials (Fig. 7.6). Apparently, the clay containing PA6 component

Table 7.9 Longitudinal tensile properties in UDP MFC containing various amounts and types of MMT and obtained with and without preblending

Composition HDPE/PA6 MMT/YP wt%	Vol. fract. of PA6/ MMT V_f	E (MPa)	ΔE (%)	σ_{max} (MPa)	$\Delta\sigma_{max}$ (%)
100/0/0		825 ± 10	0	26 ± 1	z‘
1 NM 82	0.169	1015 ± 28	23	32 ± 2	21
2.5 NM 82	0.167	1072 ± 17	30	37 ± 1	40
4 NM 82	0.164	1166 ± 22	41	48 ± 3	81
4 NM 82 IS	0.164	1078 ± 14	31	42 ± 2	59
4 CL 82	0.164	1104 ± 41	34	43 ± 3	62
4 CL 82 IS	0.164	1077 ± 15	30	46 ± 2	74
5 NM 82	0.163	1191 ± 27	44	48 ± 4	81
5 NM 82 IS	0.163	1159 ± 24	40	45 ± 3	70
5 CL 82	0.163	1161 ± 21	41	53 ± 2	100
5 CL 82 IS	0.163	1149 ± 23	39	42 ± 3	58
7.5 NM 82	0.159	1244 ± 16	51	39 ± 2	47
0% MMT	0.171	1092 ± 52	32	57 ± 4	119
80/20/0					
1 NM 722	0.169	1020 ± 40	24	37 ± 2	40
2.5 NM 722	0.167	1094 ± 46	33	42 ± 3	58
4 NM 722	0.164	1196 ± 25	45	54 ± 4	104
4 NM 722 IS	0.164	1156 ± 32	40	49 ± 3	84
4 CL 722	0.164	1170 ± 24	42	52 ± 3	96
4 CL 722 IS	0.164	1101 ± 21	33	45 ± 2	70
5 NM 722	0.163	1215 ± 24	47	59 ± 1	123
5 NM 722 IS	0.163	1147 ± 34	39	43 ± 2	62
5 CL 722	0.163	1187 ± 12	44	55 ± 4	108
5 CL 722 IS	0.163	1138 ± 10	38	43 ± 2	62
7.5 NM 722	0.160	1288 ± 27	56	44 ± 4	66
0% MMT	0.171	1030 ± 19	25	45 ± 3	73
77.5/20/2.5					

Sample designations are according to Table 7.8. The values of the neat HDPE matrix and of the UDP MFC without MMT are also presented for comparison.

reinforces most effectively in fibrillar form with stronger effect if continuous parallel fibrils are present.

The systematic research on the flexural stiffness C_R of cross-ply composites (CPC) with dual reinforcement revealed improvement of 8%–10% in respect to the CPC analogues without clay only at the highest loads of 7.5 NM reaching values of 2.9 GPa. The dually reinforced CPC with clay content of 5 wt% showed C_R values in the

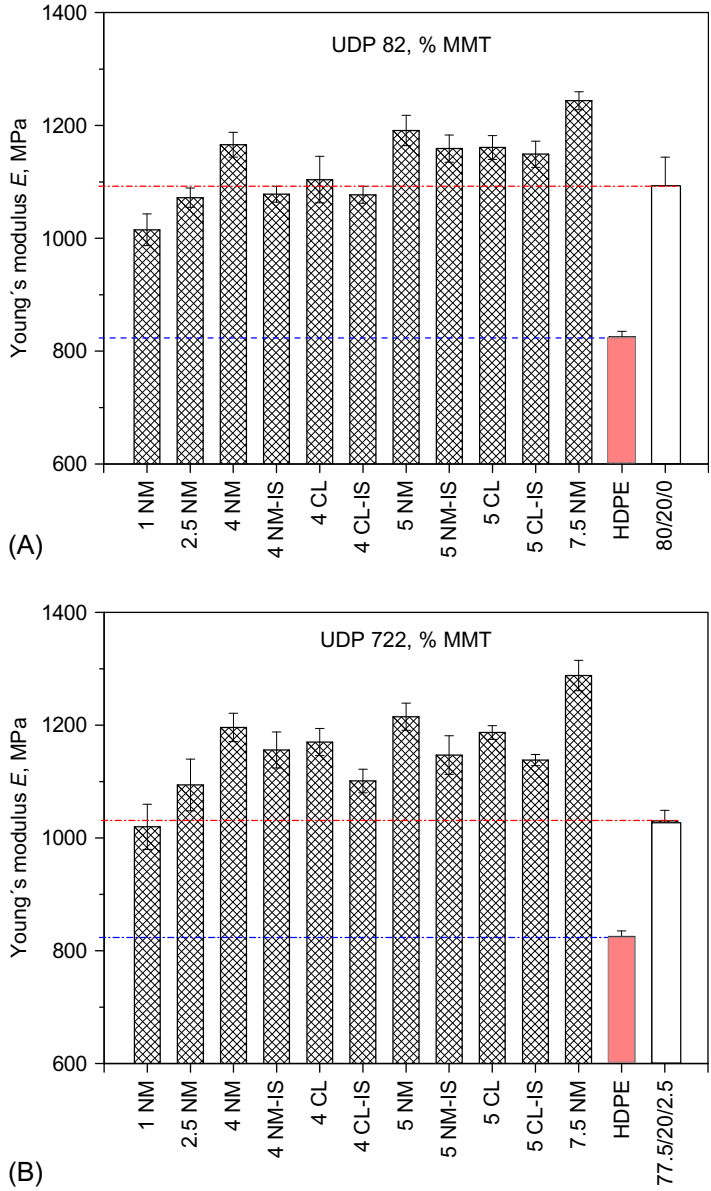

Fig. 7.19 Longitudinal Young's moduli *E* of UDP (A, B) and MRM

Continued

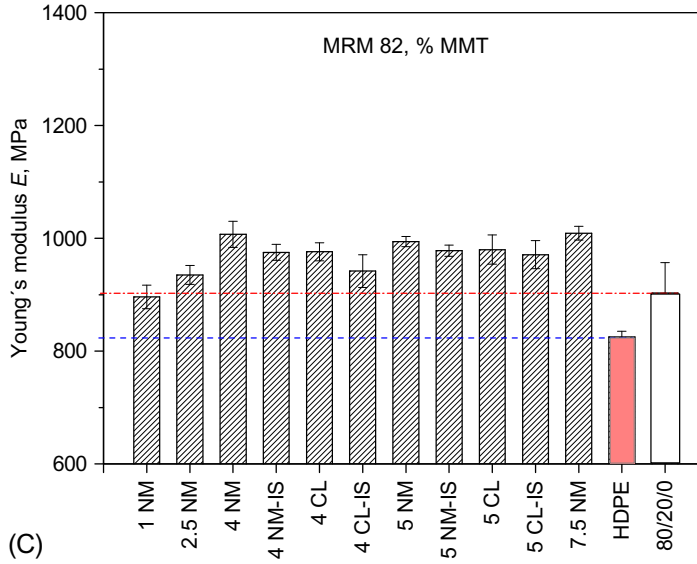

Fig. 7.19, cont'd (C) composites based on HDPE/PA6-MMT/YP samples containing various amounts and types of MMT obtained with and without premixing in the stage of extrusion. For sample designation see Table 7.8. The designation of the MMT types and concentrations are given in Table 7.5. The HDPE matrix values and those of the UDP MFC without MMT (80/20/0 and 77/20/2.5) are presented for comparison.

2.2–2.6 GPa range. Generally, increasing the clay amount, applying premixing and 2.5% of compatibilizer influences positively the C_R values [55].

The impact properties of the CPC with clay were also tested reaching the conclusion that for all systems studied the peak impact energy was significantly lower than in the HDPE matrix material. The total impact energy, however, is closer or even slightly higher, especially in the samples comprising 1% NM and 4% of CL, both without and with compatibilization. The physical meaning of these results is that in the studied CPC composites the sample failure starts at lower energy levels, but the crack propagation requires more energy before the total failure, apparently due to the presence of reinforcing fibrils [55]. It can be concluded that the positive changes in the tensile and flexural behavior of the CPC systems with additional clay reinforcement are accompanied by reasonable impact behavior, without considerable deterioration due to the clay presence. The CL clay seems to perform slightly better than NM, i.e., some relation to the chemical treatment of the clay could be present. Using minimum clay loads of 1% in the PA6 seems to cause better impact properties in the CPC, which might be related to the higher degree of clay exfoliation in this case [61].

All of the above results on CPC laminates with additional MMT reinforcement of the PA6 microfibrils are not optimized. For optimization of these composites systematic studies on the influence of the ply number, their configurations and geometries are needed.

7.3.2.2 Morphological studies

The morphological studies of the dually reinforced HDPE/PA6-based unidirectional MFC started with SEM and WAXS studies designated to elucidate the fibrillary structure of the PA reinforcement and the nature and parameters of the TCL at the fibril/matrix interface. The SEM micrographs in Fig. 7.20 allow the observation of the visible average diameters of the MMT-loaded PA6 microfibrils in two selected dually reinforced UDP, namely 5 NM 82 (Fig. 7.20A) and 5 NM 722 (Fig. 7.20B).

Table 7.10 includes data about the evolution of the PA6 structural entities during the extrusion and cold drawing of the HDPE/PA6-MMT/YP blends. The evaluation of the sizes of the PA6-MMT droplets and fibrils along the extruder line and in the final UDP was performed using the SEM microscope software measuring 5–10 structural entities in every micrograph.

The data in Table 7.10 show that, in general, the fibrils' diameters D_3 of the final UDP are significantly smaller as compared to D_1 and D_2 in the respective samples taken at the extruder die (D_1) and first haul-off (D_2). This means effective orientation of the PA6 component during the cold drawing. The samples without YP display thicker fibrils than in the compatibilized ones. The in situ preparation of the oriented precursors (i.e., without preblending of the masterbatch with neat PA6) seems to produce thinner fibrils as well. The UDP composites that showed the highest Young's moduli and strengths contain relatively thick fibrils with D_3 in the 1.2–2.6 μm range. Expectedly, increasing the MMT content in the PA6 fibrils resulted in a growth in their D_3 in the UDP without YP, however upon compatibilization with 2.5% of YP the fibrils became thinner. It should be noted that the fibrils in most of the non-compatibilized UDP prepared with preblending look like ribbons and that in some UDP samples the fibrils seem as having been subjected to plastic deformation during the cryofraction [55].

In none of the micrographs used to produce the data in Table 7.10 can one observe the entire length of a reinforcing fibril so as to determine its aspect ratio, even after

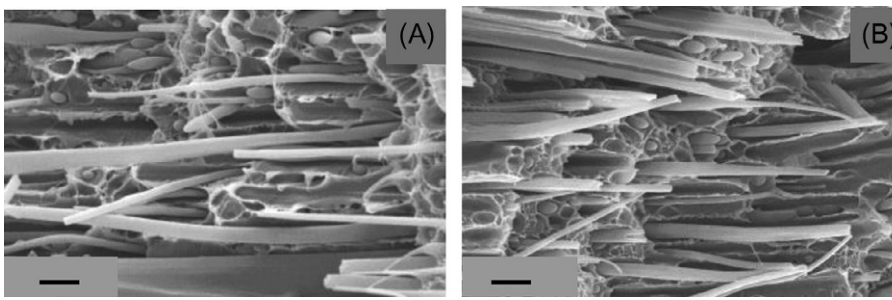

Fig. 7.20 Selected SEM images of dually reinforced UDP MFC without and with YP with 5% NM (preparation with preblending): (A) 5 NM 82; (B) 5 NM 722. For sample designation, see Table 7.8. The scale bar in the images corresponds to 5 μm.
Modified from Motovilin M. Development and investigation of new hybrid composite materials based on oriented blends of thermoplastic polymers and nanosized inorganic fillers [Ph.D. thesis]. University of Minho; 2011. https://repositorium.sdum.uminho.pt/bitstream/1822/14250/1/Thesis_Mladen%20Motovilin_2011.pdf.

Table 7.10 Dimensions of the PA6-MMT formations in the HDPE matrix at different stages of the dually reinforced MFC preparation as established by SEM observation

Composition[a]	At the die exit D_1, (μm)	After haul-off 1 D_2, (μm)	In UDP MFC D_3, (μm)
4 NM 82	**3.75 ± 0.27**	**2.70 ± 0.21**	**2.60 ± 0.21**
4 NM 82 IS	3.70 ± 0.21	2.65 ± 0.24	2.10 ± 0.17
4 CL 82	2.00 ± 0.13	1.70 ± 0.11	1.60 ± 0.12
4 CL 82 IS	2.00 ± 0.17	1.80 ± 0.15	1.40 ± 0.07
5 NM 82	**3.15 ± 0.22**	**2.00 ± 0.10**	**1.45 ± 0.04**
5 NM 82 IS	3.00 ± 0.19	2.05 ± 0.16	1.40 ± 0.06
5 CL 82	**2.95 ± 0.24**	**1.75 ± 0.13**	**1.32 ± 0.12**
5 CL 82 IS	2.45 ± 0.15	1.80 ± 0.09	1.15 ± 0.08
7.5 NM 82	3.35 ± 0.28	2.15 ± 0.20	1.75 ± 0.09
4 NM 722	**3.30 ± 0.23**	**1.90 ± 0.14**	**1.75 ± 0.11**
4 NM 722 IS	2.40 ± 0.11	1.40 ± 0.12	1.20 ± 0.05
4 CL 722	1.60 ± 0.09	0.90 ± 0.03	0.80 ± 0.03
4 CL 722 IS	0.90 ± 0.04	0.80 ± 0.02	0.70 ± 0.02
5 NM 722	**1.65 ± 0.08**	**1.35 ± 0.10**	**1.25 ± 0.06**
5 NM 722 IS	1.85 ± 0.12	1.65 ± 0.08	1.55 ± 0.14
5 CL 722	**1.25 ± 0.07**	**1.30 ± 0.04**	**1.20 ± 0.04**
5 CL 722 IS	1.55 ± 0.03	1.40 ± 0.05	1.15 ± 0.07
7.5 NM 722	2.90 ± 0.19	1.30 ± 0.07	1.10 ± 0.05

[a] The highlighted compositions showed best performance in the tensile tests [55].

selective dissolution of the HDPE. As regards the microfibrils' genesis, based on their studies on PP/PET blends with compositions close to 50/50 wt%, Fakirov et al. [63] stated that the fibril formation in MFC should be attributed mostly to coalescence of globules of the reinforcing component and not to their deformation. It should be noted, however, that in the HDPE/PA6 blends the fibril-forming PA6 component goes only to 20 wt%, which makes the coalescence less probable, especially when taking into account that a cold drawing is performed far below the melting temperature of PA6. An alternative way of PA microfibril formation based predominantly on the deformation of the PA component globules was also hypothesized [36]. It is believed that the formation of the fibrils in MFC should be a result of superposition of both mechanisms. Which one will prevail should depend on the physical properties of both matrix and reinforcing components and on the conditions (mostly temperature of drawing and draw ratio) used in the extruder line.

7.3.2.3 Combined microscopy and X-ray studies

The data about the microfibril visible diameters obtained from SEM and the WAXS data treatment described by Eqs. (7.1)–(7.8) were used to quantify the parameters of the TCL in dually reinforced UDP applying the same methodology as in the systems without clay (Fig. 7.11). The total scattering $\Phi(s,\chi)$ from the two-dimensional WAXS

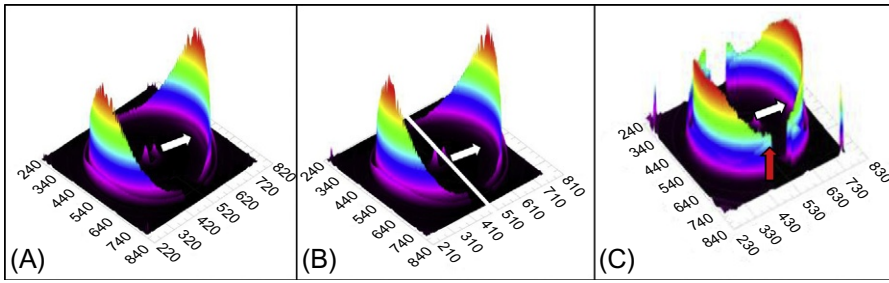

Fig. 7.21 3D WAXS patterns of three dually reinforced UDP after subtraction of the azimuthally independent component of the total scattered intensity: (A) 5 NM 82; (B) 5 CL 82 and (C) 7.5 NM 82 at 30°C. The white arrows point at the equatorial reflections of PA6.The white line in image b indicates the fibril's axis direction which is the same for the three samples. The dark arrow points at the meridional (200) refection of HDPE in (C) that is missing in (A) and (B) [55].

patterns of the UDP was divided into two components. As previously discussed, in theory, the isotropic part $\Phi_{iso}(s)$ would originate mostly from the nonoriented semi-crystalline HDPE bulk matrix material with some MMT isotropically dispersed in it, as well as from the amorphous fraction of PA6. The oriented $\Phi_{aniso}(s,\chi)$ scattering belongs to the fibril components comprising PA6, MMT and transcrystalline HDPE reflections, all of these reflections being oriented, i.e., azimuthally dependent.

Fig. 7.21 shows the 3D WAXS patterns of three UDP samples, namely 5 NM 82, 5 CL 82 and 7.5 NM 82, in which $\Phi_{aniso}(s,\chi)$ is projected on the vertical. The white arrows point at the angular position of the PA6 oriented reflections. Due to the lesser scattering capability of PA6, its reflections are less intense than the strong HDPE peaks belonging to the (110) and (200) planes of the orthorhombic HDPE. The latter appear at the equator (i.e., perpendicular to the fiber axis denoted by the white line in Fig. 7.21B). In the UDP with 5% of NM or CL (Fig. 7.21A and B), the (200) and (002/202) reflections of α-PA6 also appear on the equator. This is a clear indication for epitaxial crystallization of oriented HDPE matrix material upon the oriented PA6 reinforcing fibrils forming a TCL in which the crystallites are aligned predominantly along the fiber axis as found in the HDPE/PA6/YP UDP composites without MMT. Increasing the MMT content in the oriented PA6 to 7.5% (Fig. 7.21C) results in partial reorientation of a significant part of the intensity of the two main HDPE reflections along the meridian (the dark arrow in Fig. 7.21C). Note that the meridional (110) peak of HDPE was truncated during the so-called "Fraser correction" of the WAXS image. It can be therefore concluded that above a certain concentration the MMT in the dually reinforced UDP samples can change the orientation of the TCL.

For a quantitative evaluation of the oriented and isotropic parts of the total scattered intensities of all UDP samples, the respective 2D WAXS patterns were integrated along their radii in the 0–180 degrees range to get the 1D WAXS profiles, which were afterwards deconvoluted by fitting with Gaussian peaks. Fig. 7.22 shows an example of the fitting of the aniso- and iso-fractions of WAXS in the case of the 4 NM 82 UDP.

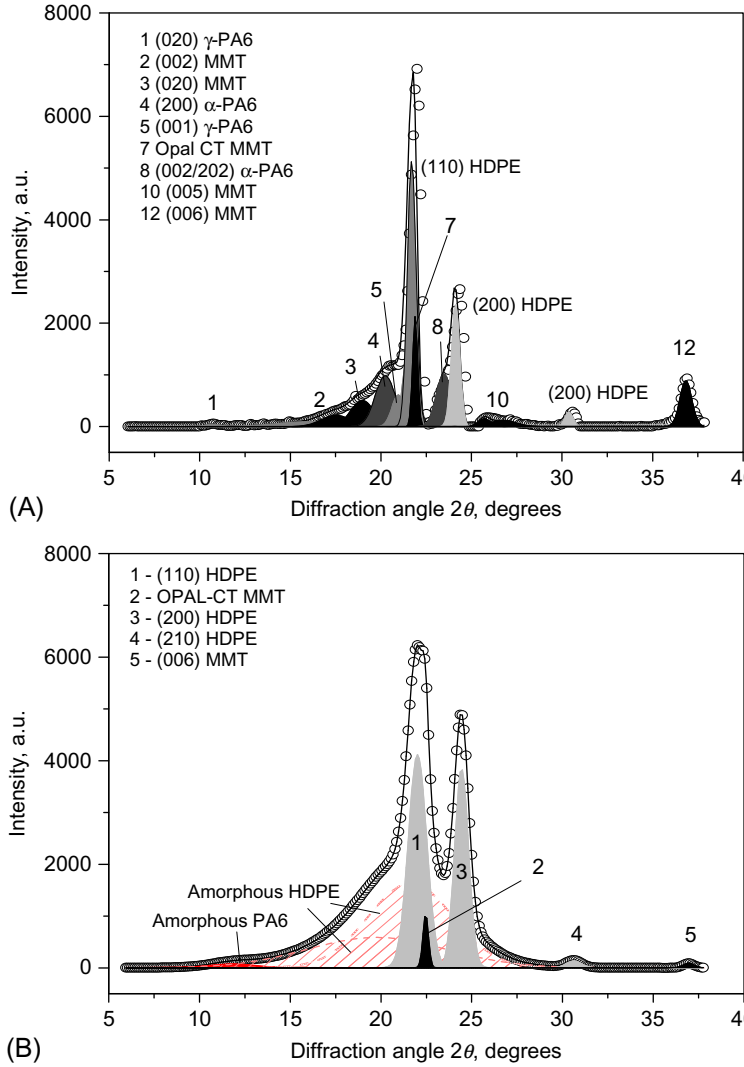

Fig. 7.22 Example of peak fitting for 4 NM 82 UDP sample after separation of the total WAXS into: (A) $\Phi_{aniso}(s)$ and (B) $\Phi_{iso}(s)$. The latter does not contain isotropic PA6 reflections. Modified from Motovilin M. Development and investigation of new hybrid composite materials based on oriented blends of thermoplastic polymers and nanosized inorganic fillers [Ph.D. thesis]. University of Minho; 2011. https://repositorium.sdum.uminho.pt/bitstream/1822/14250/1/Thesis_Mladen%20Motovilin_2011.pdf.

The correct fitting of the linear WAXS patterns and calculation of the HDPE/PA6 ratio in the fibrils was only possible knowing the positions of the crystalline peaks of MMT disclosed in Fig. 7.17, and of the α- and γ-PA6 polymorphs in the PA6/o-MMT hybrids (Fig. 7.18). Detailed analysis of these data is given in Ref. [55]. Here only the main structural conclusions drawn on its basis will be presented.

Let's analyze first the isotropic WAXS exemplified in Fig. 7.22B. In theory, it should contain reflections of nonoriented HDPE bulk matrix and certain nonoriented PA6 scattering. Deconvolution of all iso-patterns of UDP showed that in the samples without YP compatibilizer there is no nonoriented PA6 scattering. It appears in the samples with YP and increases with the MMT content reaching its maximum of 11% in the sample with 7.5% MMT.

Interestingly, the iso-scattering of all dually reinforced UDP contains also MMT reflections, e.g., the (006) reflection as seen in Fig. 7.22B. In the 4 NM 722 and 4 CL 722 samples the in situ preparation leads to significantly higher amounts of isotropic MMT as compared to the preblending method. In the noncompatibilized ones 4 NM 82 and 4 CL 82 these concentrations are similar for all composites studied.

The presence of PA6 reflections in the isotropic WAXS of some samples indicates that the reinforcing fibrils in them were not completely oriented. Apparently, the highest possible draw ratio not causing rupture of the respective OC precursors has been insufficient for complete PA6 fibrillation and left a fraction of nonoriented PA6 found probably in the core of the fibrils transported into the respective UDP. Consequently, in these samples the isotropic MMT will be found predominantly in the isotropic PA6 fibril core (in the samples with preblending), or also in the isotropic HDPE matrix for the IS samples. In the UDP not containing isotropic PA6, the appearance of some reflections of MMT in the iso-WAXS could only be due to MMT migration from the fibrils to the matrix.

Fig. 7.22A shows an example of deconvolution of the oriented WAXS in the noncompatibilized 4 NM 82 UDP sample. This linear WAXS profile is not expected to display diffuse scattering (halos) but only crystalline peaks of PA6, MMT, and HDPE. The physical meaning of this is that any orientation of the matrix or fibril materials would cause crystallization, which is acceptable for such strongly crystallizable polymers as HDPE and PA6. As expected, the oriented fraction of WAXS in all UDP samples is richer in PA6, the PE/PA6 relation being in the range of 0.15–0.36 (no YP) and 0.14–0.50 (2.5% YP). The PE percentage comprises the oriented transcrystalline HDPE from the matrix in the noncompatibilized samples while in the compatibilized ones it will include also the PE material from the YP compatibilizer, which, being chemically bonded to the PA6 fibril, will unavoidably be a part of the TCL.

Similarly to the analysis for MFC without clay (Section 7.2.3.3, Table 7.4) calculations of the TCL thickness based on combined WAXS/SEM results were made for UDP systems with clay. Table 7.11 presents this information for two compositions HDPE/PA6/YP with different MMT content. Data for E, σ_{max}, and C_R are also presented. It can be seen that the compatibilizer, the clay amount and type affect significantly the TCL thickness. Thus, in the noncompatibilized 5 NM 82 and 5 CL 82 the TCL thicknesses are 173 and 72 nm, respectively, producing quite similar E values of c.1200 MPa and high C_R values of 2.4–2.5 GPa, σ_{max} being higher in the latter case. Clay load of 7.5% NM is related to some decrease in the TCL thickness as compared to the sample with 5% NM, resulting in superior E modulus and flexural properties but a drop in the tensile strength. The 7.5 NM 82 sample displayed one of the thickest PA6 fibrils obviously due to a lower orientation in the cold drawing stage of preparation. Introducing 2.5% of YP compatibilizer results in significantly finer fibrils as revealed

Table 7.11 Dependence between the morphological parameters of the fibrils (R_2, R_1 and TCL) calculated from WAXS or determined from SEM data and the mechanical behavior in various HDPE/PA6/YP composites containing various amounts and types of MMT nanoclays [44]. See also Fig. 7.13 and the text.

	80/20/0 + MMT			77,5/20/2,5 + MMT		
	5 NM 82	7.5 NM 82	5 CL 82	5 NM 722	7.5 NM 722	5 CL 722
$2R_2$, (nm)	1450	1750	1320	1250	1100	1200
$2R_1$, (nm)	1104	1508	1176	923	984	1100
TCL = R_2–R_1	173	121	72	164	58	50
E_1, (MPa)	1191	1244	1161	1215	1288	1187
σ_{max}, (MPa)	45	39	53	59	56	55
C_R, (MPa)	2500	2850	2420	2590	2950	2340

by SEM, i.e., lower $2R_2$ values and finer TCL, strongly depending on the clay amount and type. In the NM-containing compatibilized UDP the σ_{max} values increase, the difference in E_1 and C_R depending more on the amount than on the type of the clay.

Comparing the data in Tables 7.4 and 7.11, it can be concluded that the thickness of TCL in the noncompatibilized samples without MMT (Table 7.4) seems to be inversely proportional to the tensile strength. In these samples the thinner TCL can result in higher E_1 and C_R values since its dampening effect will be lower. In the dually reinforced MFC (Table 7.11) this effect is the opposite most probably due to possible migration of MMT from the PA6 fibrils into the TCL. Compatibilization with YP, in general, results in thinner TCL, whereby in the samples without MMT (Table 7.4) all mechanical properties deteriorate. This is not the case in the dually reinforced MFC in Table 7.11 which can be explained with the different composition and special orientation of the TCL in the dually reinforced UDP samples, especially at higher clay loads. Moreover, in the systems without YP compatibilizer the formation of TCL would involve HDPE matrix material only. In the compatibilized UDP, however, a chemical reaction between the maleic anhydride of YP and the amide groups of PA6 may be expected during MFC preparation [24]. There, the TCL will include polyolefin component from the YP compatibilizer, which is different from the bulk matrix HDPE and most probably modifies the adhesion at the matrix-fibril interface.

7.3.2.4 *Simultaneous straining/small angle X-ray scattering*

Data about the simultaneous straining/SAXS experiments in various MFC with composition HDPE/PA6/YP = 80/20/0 are presented in Fig. 7.23. The structures of the HDPE from TCL in MFC at 30°C with and without MMT (Fig. 7.23A and C, respectively) as presented by the moduli of the respective CDF functions, seem to be quite similar. After eliminating the HDPE reflections from TCL by heating at 160°C

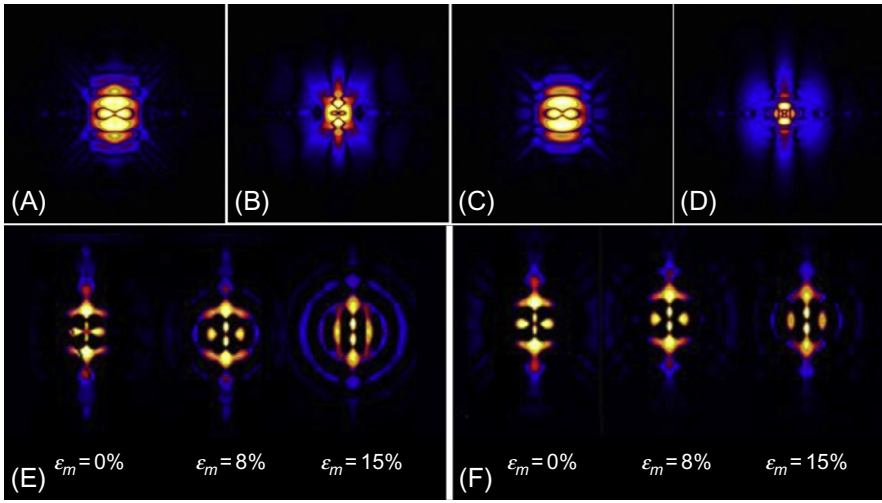

Fig. 7.23 CDF images $|z(r_{12},r_3)|$ of various MFC with composition HDPE/PA6/YP = 80/20/0: (A) with 5% NM, at 30°C; (B) same as (A), at 160°C; (C) no MMT, at 30°C; (D) no MMT, at 160°C; (E) with 5% NM strained at 30°C; (F) with 5% CL15A strained at 30°C; Images (A) trough (D) present both negative and positive faces of CDF; (E) and (F) present the CDF faces. The fiber axis and strain direction are vertical [44].

(Fig. 7.23B and D), it appears that the PA6 microfibrils containing MMT (Fig. 7.23B) are built of longer and straighter crystalline domains. This makes the interfibrillar distance shorter than in the respective UDP MFC without MMT (Fig. 7.23D). Such an effect seems to be natural: a bunch of the wavy microfibrils of the MFC without MMT must maintain a wider distance from each other compared to a bunch of straight fibrils. Moreover, in the sample with MMT the off-meridional peaks indicate some lateral correlation among the PA6 crystallites suggesting arrangement in a rudimental 3D lattice, in which the PA6 domains vary in the range of 9–10 nm.

Fig. 7.23 displays also the negative part of CDF computed from the oriented SAXS in two MFC samples containing 5% of NM (Fig. 7.23E) and CL15A (Fig. 7.23F) in a straining experiment at 30°C. Three different stages of the straining process are considered: before deformation ($\varepsilon_m = 0$), toward the middle of the straining ($\varepsilon_m =$ 8%–9%), and at a certain point before the sample failure at $\varepsilon_m = 13\%–15\%$. In equatorial direction one observes even at $\varepsilon_m = 0$ peaks with long spacings $L = 12–14$ nm growing up to c.20 nm as the strain increases. These peaks can be attributed to lateral correlation of HDPE tip and satellite domains, as in the samples without clay (Fig. 7.16). In the present case, however, these satellite domains are not a result of strain-induced crystallization because they are present before application of strain. At $\varepsilon_m = 0$, the positioning of the satellite and tip domain is frontal since the equatorial reflections are almost point-like. At $\varepsilon_m = 14\%–15\%$ this arrangement is distorted (better expressed in the NM-containing sample) reflected by the formation of arcs.

In axial direction the two samples with display correlation of at least three narrow HDPE domains. Interestingly, the PA6 peaks are also clearly observable in the negative faces even at 30°C as two bright points on the meridian, right in the center of the images.

Fig. 7.24A–D display the evolution of the mechanical and nanostructural parameters during the continuous straining of the four UDP MFC with different compositions and clay reinforcement. Comparing the samples with 5% NM or CL (Fig. 7.24A and B) shows that the stress at break values are similar, being in the range of 44–45 MPa, i.e., comparable to the respective values from the mechanical tests in Table 7.9. The 5 CL 82 sample is less ductile with a macrodeformation before break of 11%, while in 5 NM 82 it reaches 26%. These percentages are calculated on the basis of the constant strain rate [51]. As to the nanostructural parameters, in both samples the starting values of the HDPE long period of the TCL (L_m^{HDPE}) are close to 22–24 nm and increase gradually as the strain grows reaching values of 30 nm. The long period of the isotropic matrix material $L_{\mathrm{iso}}^{\mathrm{HDPE}}$ (not shown in Fig. 7.24) is independent of strain and remains constant close to 25 nm in the two composites with 5% nanoclay. The long period L_{eq}^{HDPE} of the laterally correlated HDPE domains is in the range of 12–13 nm even before any strain. Then it grows to 17 nm just before sample failure. It could be therefore concluded that the presence of nanoclay in the PA6 fibrils results in the formation of HDPE satellite domains, as in the process depicted in Fig. 7.16. In this case, however, it occurs not only as a result of strain, but even in the stage of MFC preparation. As to the long period of the PA6 domains L_m^{PA6}, continuous deformations in the range of 15%–26% led to its small increase from 8 to 10 nm. The lateral extent of the HDPE domains decreases slightly for both samples, which is opposite to what was observed with the MFCs without nanoclay (Fig. 7.14).

Fig. 7.24 shows also the structure-properties relationship in 7.5 NM 82 and 7.5 NM 722 samples under strain. The noncompatibilized sample (Fig. 7.24C) shows higher deformability reaching ε_{mb} of 27% and $\sigma_{\max}$ of 32 MPa, while for the MFC with 2.5% YP (Fig. 7.24D) the respective values are $\varepsilon_{mb} = 11\%$ and $\sigma_b = 35$ MPa. The meridional long period of the HDPE from TCL L_m^{HDPE} is only seen in the compatibilized sample (Fig. 7.24C), growing from 22 to 27 nm during the straining experiment. The noncompatibilized sample (Fig. 7.24C) did not display the L_m^{HDPE} periodicity due to CDF peak superposition. Both UDP with 7.5% NM show an equatorial long spacing L_{eq}^{HDPE}—initially between 18 and 20 nm that grows slightly as the strain increases. The nanostructure of the PA6 oriented material remains almost unchanged during the straining experiment. The L_m^{PA6} periodicities slightly fluctuate around 9.0–9.5 nm for the sample without YP (Fig. 7.24C) and 8.0–8.5 nm with YP (Fig. 7.24D). For a comparison, in the two UDP without nanoclay in Fig. 7.14A and B L_m^{PA6} varies between 6.5 and 7.2 nm, i.e., the introduction of MMT into the PA6 fibrils results in larger long periods.

Summarizing, the presence of MMT in unidirectional MFC induces irreversible crystallization in the vicinity of the TCL/fibril ensemble even without strain, thus maintaining the nanostructure of the ensemble quite constant until sample failure.

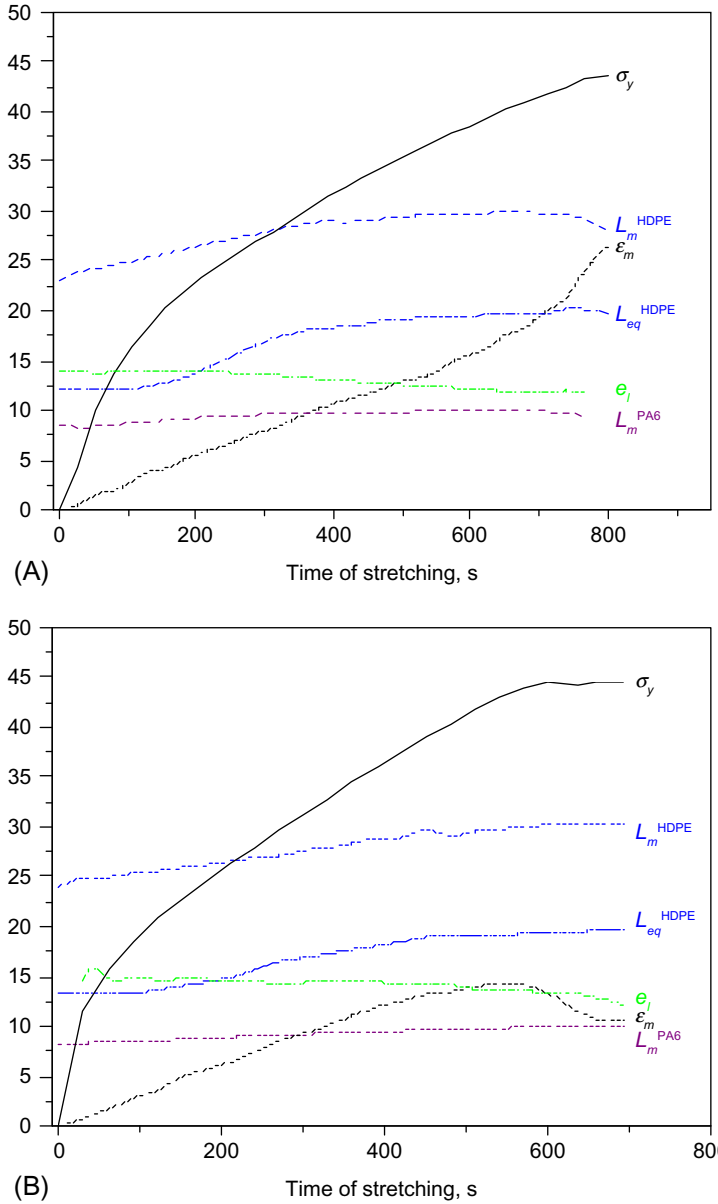

Fig. 7.24 Evolution of the nanostructural and mechanical parameters during the simultaneous SAXS/straining of various UDP MFC with different composition and clay reinforcement: (A) 5 NM 82; (B) 5 CL 82;

Continued

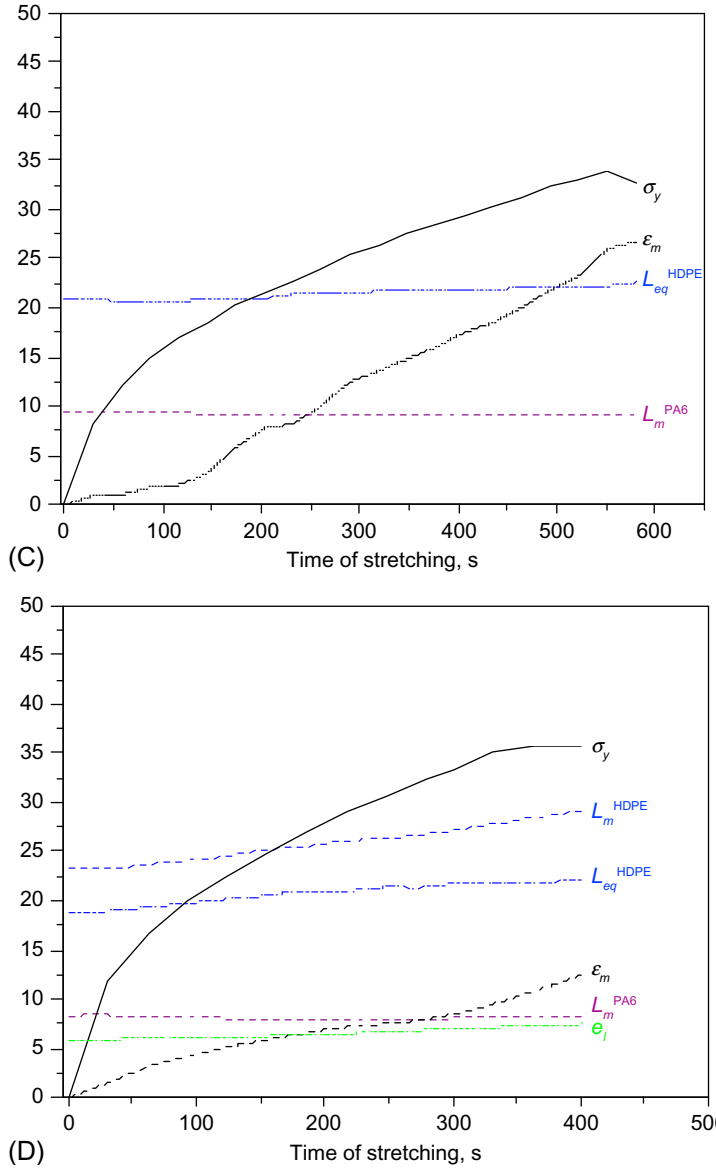

Fig. 7.24, cont'd (C) 7.5 NM C82; (D) 7.5 NM 722. The nanostructural data are obtained from the respective negative CDF peaks of the azimuthally dependent SAXS. Legend: longitudinal stress σ_y (MPa); macroscopic strain ε_m (%); meridional long period of transcrystalline HDPE domains L_m^{HDPE} (nm); equatorial long period L_{eq}^{HDPE} (nm) of stress-crystallized HDPE; meridional long period L_m^{PA6} (nm) of PA6; lateral extent e_l (nm) of the meridional transcrystalline HDPE domains [51].

7.4 Concluding remarks

Nowadays the MFC materials based on HDPE/PA blends are among the most systematically studied composites of this type. These MFC combine the strength and stiffness of two common engineering polymers providing better mechanical properties than their equivalent blends without in situ structuring. They have the potential to rival glass-reinforced composites based on PE matrices in terms of mechanical resistance. The reason for the significant reinforcement of the matrix is related with the in situ creation of microfibrillar morphology of the PA component with controllable sizes and alignment. The interfacial interaction of the PA microfibrils with the HDPE matrix is realized *via* a TCL of oriented matrix material and can be tailored through the MFC composition, as well as by the processing conditions. In such a way the technological incompatibility of PE and PA is overcome to the benefit of the mechanical properties in tension and flexure, maintaining in most of the cases reasonable impact properties. As all MFC, the HDPE/PA systems have the advantage of being manufactured using standard polymer processing techniques and equipment. One more benefit of the MFC concept is the possibility for additional strengthening of the PA reinforcing entities by nanoclays. This dual reinforcement fixes the nanostructure of the composite, thus contributing for the improvement of the tensile and flexural moduli, with expected positive changes in the barrier properties. The use of various additional fillers in MFC seems to be a pathway toward functional advanced composites with tailored properties.

Our X-ray scattering studies on HDPE/PA microfibrillar systems complemented by SEM demonstrated that static and dynamic synchrotron WAXS and SAXS methods, including in-beam stretching and heating, can be very useful in studying the relation between the MFC morphology and their mechanical properties. The new approaches for quantification of the sample nanostructure in real space based on automatic calculation and evaluation of the multidimensional CDF will expectedly become more frequently used in the future, thus increasing the quality and utility of the results returned from the X-ray scattering experiments.

There exist also large field of research related to the development of more sophisticated extruder line components such as stretching devices, dies, more sophisticated molds and other machinery useful for preparation of MFCs.

Whatever the future development in the area of MFC would be, any further development will by all means require an interdisciplinary approach, combining knowledge related to polymer chemistry and physics, polymer processing and characterization, mechanics, computerized image processing, and programming.

Acknowledgments

The authors acknowledge the support of the project TSSiPRO-NORTE-01-0145-FEDER-000015 funded by the regional operational program NORTE 2020, under the PORTUGAL 2020 Partnership Agreement, through the European Regional Development Fund. NVD also thanks for the financial support of the Portuguese Foundation for Science and Technology (FCT) in the frames of the strategic projects LA25/2013–2014 and UID/CTM/50025/2013.

References

[1] Fakirov S. The concept of micro- or nanofibrils reinforced polymer-polymer composites. In: Bhattacharyya D, Fakirov S, editors. Synthetic polymer-polymer composites. Munich: Hanser; 2012. p. 353–94.

[2] Schadler LS. Polymer-based and polymer-filled nanocomposites. In: Ajayan PM, Schadler LS, Braun PV, editors. Nanocomposite science and technology. Weincheim: Wiley-VCH; 2003. p. 77.

[3] Bank LC. Composites for construction: structural design with FRP materials. Hoboken, NJ: John Wiley & Sons; 2006. p. 7.

[4] Schwartz M. Composite materials handbook. New York: McGraw-Hill; 1984. p. 23.

[5] Evstatiev M, Fakirov S. Microfibrillar reinforcement of polymer blends. Polymer 1992;33:877–80.

[6] Evstatiev M, Fakirov S, Schultz JM. Microfibrillar reinforced composite from drawn poly(ethylene terephthalate)/nylon-6 blend. Polymer 1993;34:4669–79.

[7] Schaefer DW, Justice RS. How nano are nanocomposites? Macromolecules 2007;40: 8501–9517.

[8] Fakirov S, Evstatiev M, Friedrich K. Microfibrillar reinforced composites from polymer blends. In: Radusch HJ, Vogel J, editors. Polymerwerkstoffe 1998: verarbeiterung, anwendung, recycling. Halle/Saale: Martin-Luther-Universität, Halle-Wittenberg; 1998. p. 123–56.

[9] Fakirov S, Evstatiev M, Friedrich K. Microfibrillar reinforced composites from polymer blends. In: Paul DR, Bucknall CB, editors. Polymer blends. New York: Wiley; 2000. p. 455–76.

[10] Fakirov S, Evstatiev M, Friedrich K. Nanostructured polymer composites from polymer blends: morphology and mechanical properties. In: Fakirov S, editor. Handbook of thermoplastic polyesters. Weincheim: Wiley-VCH; 2002. p. 1093–132.

[11] Denchev Z, Dencheva N. Transforming polymer blends into composites: a pathway towards nanostructured materials. Polym Int 2008;57:11–22.

[12] Jayanarayanan K, Thomas S, Joseph K. Studies on in situ microfibrillar composites based on blends of polyolefins and polyester. Saarbrücken, Germany: LAP LAMBERT Academic Publishing; 2011.

[13] Denchev Z, Dencheva N. Preparation, mechanical properties and structural characterization of microfibrillar composites based on polyethylene/polyamide blends. In: Bhattacharyya D, Fakirov S, editors. Synthetic polymer-polymer composites. Munich: Hanser; 2012. p. 465–524.

[14] Denchev Z, Evstatiev M, Fakirov S, Friedrich K, Pollio M. Microfibrillar reinforced composites—the role of the chemical interactions at the fibril-matrix interface. Adv Compos Mater 1998;7:313–24.

[15] Lin C, Sun H, Wang S, Huang J, Li J, Guo S. In-process ultrasonic measurements of orientation and disorientation relaxation of HDPE/PA6 composites with compatibilizer. J Appl Polym Sci 2010;116:320–7.

[16] Ray SS, Okamoto M. Polymer/layered silicate nanocomposites: a review from preparation to processing. Prog Polym Sci 2003;28:1539–641.

[17] Usuki A, Hasegawa N, Kato M. Polymer-clay nanocomposites. Adv Polym Sci 2005;179: 135–95.

[18] Kamal MR, Jinnah IA, Utracki LA. Permeability of oxygen and water vapor through polyethylene/polyamide films. Polym Eng Sci 1984;24:1337–47.

[19] Utracki LA, Dumoulin MM, Toma P. Melt rheology of HDPE/PA6 blends. Polym Eng Sci 1986;26:34–44.
[20] Willis JM, Favis BD. Processing-morphology relationships of compatibilized polyolefin/polyamide blends. Part I: the effect of an ionomer compatibilizer on blend morphology. Polym Eng Sci 1988;28:1416–26.
[21] Chandramouli K, Jabarin SA. Morphology and property relationships in ternary blends of PE/PA6/compatibilizing agents. Adv Polym Technol 1995;14:35–46.
[22] Beltrame PL, Castelli A, Pasquantonio MD, Canetti M, Seves A. Influence of interfacial agents on the physicochemical characteristics of binary PE/PA and ternary PE/PP/PA6 blends. J Appl Polym Sci 1996;60:579–90.
[23] Yeh JT, Huang SS, Chen HY. Barrier resistance of PE, PE/modified PA and blends of modified PA and ethylene vinyl alcohol bottles against permeation of polar and nonpolar mixed solvents. J Appl Polym Sci 2005;97:1333–44.
[24] van Duin M, Aussems M, Borggreve RJM. Graft formation and chain scission in blends of polyamide 6 and -6.6 with maleic anhydride containing polymers. J Polym Sci A Polym Chem 1998;36:179–88.
[25] Thomas S, Groeninckx G. Reactive compatibilisation of heterogeneous ethylene propylene rubber (EPM)/nylon 6 blends by the addition of compatibilizer precursor EPM-g-MA. Polymer 1999;40:5799–819.
[26] Denchev Z, Oliveira MJ, Carneiro OS. Nanostructured composites based on polyethylene–polyamide blends. I. Preparation and mechanical behavior. J Macromol Sci Part B Phys 2004;B43:143–62.
[27] Denchev Z, Oliveira MJ, Mano JF, Viana JC, Funari SS. Nanostructured composites based on polyethylene-polyamide blends: II. Probing the orientation in polyethylene-polyamide nanocomposites and their precursors. J Macromol Sci Part B Phys 2004;43:163–76.
[28] Dencheva N, Oliveira MJ, Carneiro OS, Nunes TG, Denchev Z. Preparation and properties of novel in-situ composite materials based on polyethylene-polyamide oriented blends. Mater Sci Forum 2008;587–588:515–9.
[29] Dencheva N, Nunes T, Oliveira MJ, Denchev Z. Microfibrillar composites based on polyamide/polyethylene blends: 1. Structure investigations in oriented and isotropic PA6. Polymer 2005;46:887–901.
[30] Dencheva N, Nunes T, Oliveira MJ, Denchev Z. Crystalline structure of PA12 as revealed by solid-state ^{13}C NMR and synchrotron WAXS and SAXS. J Polym Sci B Polym Phys 2005;43:3720–33.
[31] Dencheva N, Denchev Z, Oliveira MJ, Funari SS. Relationship between crystalline structure and mechanical behavior in isotropic and oriented PA6. J Appl Polym Sci 2007;103:2242–52.
[32] Dencheva N, Denchev Z, Oliveira MJ, Nunes TG, Funari SS. Relationship between crystalline structure and mechanical behavior in isotropic and oriented PA12. J Appl Polym Sci 2008;109:288–302.
[33] Dencheva N. Development and investigation of novel in-situ reinforced nanocompo-sites based on oriented polymer blends [PhD Thesis]. University of Minho; 2008. https://repositorium.sdum.uminho.pt/bitstream/1822/9020/1/Dencheva_N%20Binder%201.pdf.
[34] Dencheva N, Oliveira MJ, Carneiro OS, Pouzada AS, Denchev Z. Preparation, structural development, and mechanical properties of microfibrillar composite materials HDPE/PA6 oriented blends. J Appl Polym Sci 2010;115:2918–32.
[35] Dencheva N, Oliveira MJ, Pouzada AS, Kearns M, Denchev Z. Mechanical properties of PA6-reinforced microfibrillar composites. Polym Compos 2011;32:407–17.

[36] Dencheva N, Denchev Z, Oliveira MJ, Funari SS. Microstructure studies of in-situ composites based on HDPE/PA12 blends. Macromolecules 2010;43:4715–26.
[37] Denchev Z, Dencheva N. Preparation, mechanical properties and structural characterization of in-situ microfibrillar composites based on oriented polyethylene/polyamide blends. In: Fakirov S, Bhattacharya D, editors. Synthetic polymer-polymer composites. Munich: Hanser Fachbuch; 2012. p. 465–522.
[38] Evstatiev M, Fakirov S, Bechtold G, Friedrich K. Structure-properties relationship in injection and compression molded microfibrillar reinforced PET/PA6 composites. Adv Polym Technol 2000;19:249–59.
[39] Powell PC. Engineering with fiber-polymer laminates. London: Chapman & Hall; 1994. p. 23.
[40] Nunes JP, Pouzada AS, Bernardo CA. Stiffness of anisotropic composite plates in bending. Polym Test 2002;21:27–33.
[41] Liu T, Wang Q, Xie Y, Lee S, Wu Q. Effects of use of coupling agents on the properties of microfibrillar composite based on high-density polyethylene and polyamide-6. Polym Bull 2014;71:685–703.
[42] Quan H, Li ZM, Yang MB, Huang R. On the transcrystallinity in semicrystalline polymer composites. Compos Sci Technol 2005;65:999–1021.
[43] Evstatiev M, Nikolov N, Fakirov S. Morphology of microfibrillar reinforced composites PET/PA 6 blend. Polymer 1996;37:4455–63.
[44] Dencheva N, Stribeck A, Denchev Z. Nanostructure development in multicomponent polymer systems and its characterization by X-ray scattering. Eur Polym J 2016;81:447–69.
[45] Friedrich K, Ueda E, Kamo H, Evstatiev M, Krasteva B, Fakirov S. Direct electron microscopic observation of transcrystalline layers in microfibrillar reinforced polymer-polymer composites. J Mater Sci 2002;37:4299–305.
[46] Li Z-M, Li L, Shen K-Z, Yang M-B, Huang R. In situ poly(ethylene terephthalate) microfibers- and shear-induced non-isothermal crystallization of isotactic polypropylene by on-line small angle X-ray scattering. Polymer 2005;46:5358–67.
[47] Ran S, Zong X, Fang D, Hsiao BS, Chu B, Cunniff PM, et al. Study of the mesophase in polymeric fibers during deformation by synchrotron SAXS/WAXD. J Mater Sci 2001;36:3071–7.
[48] Ruland W. X-ray determination of crystallinity and diffuse disorder scattering. Acta Cryst 1961;14:1180–5.
[49] Stribeck N. X-ray scattering of soft matter. Heidelberg, New York: Springer-Verlag; 2007.
[50] Stribeck N. Extraction of domain structure information from small-angle scattering patterns of bulk materials. J Appl Crystallogr 2001;34:496–503.
[51] Denchev Z, Dencheva N, Funari SS, Motovilin M, Schubert T, Stribeck N. Nanostructure and mechanical properties studied during dynamical straining of microfibrillar reinforced HDPE/PA blends. J Polym Sci B Polym Phys 2010;48:237–50.
[52] Zeinolebadi A, Stribeck N, Ganjaee-Sari M, Dencheva N, Denchev Z, Botta S. Nanostructure evolution mechanisms during slow load-cycling of oriented HDPE/PA microfibrillar blends as a function of composition. Macromol Mater Eng 2012;297:1102–13.
[53] Dencheva N, Denchev Z, Motovilin M, Zeinolebadi A, Stribeck N, Funari SS, et al. Nanostructure development and its relation to mechanical properties in microfibrillar composites by means of simultaneous x-ray/straining studies. Macromol Mater Eng 2013;298:1100–16.
[54] Strobl G. The physics of polymers: concepts for understanding their structures and behavior. Berlin: Springer; 2007. p. 216–220.

[55] Motovilin M. Development and investigation of new hybrid composite materials based on oriented blends of thermoplastic polymers and nanosized inorganic fillers [PhD Thesis]. University of Minho; 2011. https://repositorium.sdum.uminho.pt/bitstream/1822/14250/1/Thesis_Mladen%20Motovilin_2011.pdf.
[56] Kelnar I, Fortelný I, Kaprálková L, Hromádková J. Effect of nanofiller on fibril formation in melt-drawn HDPE/PA6 microfibrillar composite. Polym Eng Sci 2015;55:2133–9.
[57] Kelnar I, Kaprálková L, Kratochvíl J, Padovec Z, Růžička M, Hromádková J. Effect of layered silicates and reactive compatibilization on structure and properties of melt-drawn HDPE/PA6 microfibrillar composites. Polym Bull 2016;73:1673–88.
[58] Liu H, Wu Q, Zhang Q. Preparation and properties of banana fiber-reinforced composites based on high density polyethylene (HDPE)/Nylon-6 blends. Bioresour Technol 2009;100:6088–97.
[59] Liu H, Yao F, Xu Y, Wu Q. Novel wood flour filled composite based on microfibrillar highdensity polyethylene (HDPE)/Nylon-6 blends. Bioresour Technol 2010;101:3295–7.
[60] Lincoln DM, Vaia RA, Wang ZG, Hsiao BS. Secondary structure and elevated temperature crystallite morphology of nylon-6/layered silicate nanocomposites. Polymer 2001;42:1621–31.
[61] Motovilin M, Denchev Z, Dencheva N. On the structure-properties relationship in montmorillonite-filled polyamide 6 nanocomposites. J Appl Polym Sci 2011;120:3304–15.
[62] Guthrie GD, Bish DL, Reynolds RC. Modeling the X-ray diffraction pattern of Opal-CT. Am Mineral 1995;80:869–72.
[63] Fakirov S, Bhattacharyya D, Lin RJT, Fuchs C, Friedrich K. Contribution of coalescence to microfibril formation in polymer blends during cold drawing. J Macromol Sci Phys 2007;2007:183–94.

Zlatan Zlatev Denchev, Dr., DSc Received his Master degree in organic synthesis and analysis at the University of Chemical Technologies in Burgas, Bulgaria and the PhD degree from the University of Chemical Technologies and Metallurgy in Sofia, Bulgaria. Since 2000 is professor at the University of Minho, Portugal. His research interests include new strategies for the synthesis of polymer hybrids with tailored properties, as well as the characterization of multicomponent polymer systems by advanced X-ray scattering techniques.

Nadya Vassileva Dencheva, Dr. Received her Master degree in organic synthesis from the University of Chemical Technologies in Burgas, Bulgaria and her PhD in the area of polymer science and technology from the University of Minho, Portugal. Her research focuses on the synthesis of polymer hybrids from blends and by micro- and nanoencapsulation, their reactive processing and studying the structure-properties relationship in multicomponent polymer systems.

The book provides information on MFC and NFC based on polymer blends that have been accumulated over the last 25 years, offering useful reference resource for scientists and practitioners working in the areas of polymer composites, general polymer science, polymer technology, materials science, and nanotechnology. It adopts a diverse and novel approach in terms of understanding the relationship between processing, morphology, structure, properties, and applications of micro/nano-fibrillar composites and in-situ composites. Throughout the book there is a strong emphasis on the importance of developing cost-effective and environmentally-friendly microfibrillar and nano-fibrillar composites using waste plastics streams. This book covers the recycling of micro/nano-fibrillar plastic waste streams. For several decades, plastic technology has played an important role in many industrial applications such as packaging, automobiles, aerospace, and construction. However, the increasing use of plastics creates a great deal of waste. This has led to restrictions on the use of some plastics for certain applications and a drive towards recycling of plastics. *Micro and Nanofibrillar Composites (MFCs and NFCs) from PolymerBlends is a* comprehensive reference for researchers, students, and scientists working in the fields of plastics recycling and composites. The book aims to determine the influence of microfibrillar and nanofibrillar morphology on the properties of immiscible blend systems. Chapters cover microfibrillar and nanofibrillar composites, based on polyolefine, liquid crystal polymer, biodegradable polymers, polyester, and polyamide blends in various industrial application fields. The book brings together panels of highly accomplished experts in the fields of plastics recycling, blends, and composites systems.

Raghvendra Kumar Mishra is Visvesvaraya Senior Research Fellow at the International and Inter University Centre for Nanoscience and Nanotechnology, Mahatma Gandhi University, India. He received his M.Tech. in Materials Science and Technology from the Indian Institute of Space Science and Technology (ISRO), India in 2015. His specialized areas of research include polymer recycling, polymer blends, fiber-filled polymer composites, particulate-filled polymer composites, micro/nanofibrillar composites and in-situ composites, carbon nanotubes, graphene, and conducting polymer blends and composites and their morphological, physical, and chemical characterization.

Sabu Thomas is Professor of Polymer Science and Engineering at the School of Chemical Sciences, as well as Director of the Centre for Nanoscience and Nanotechnology, Mahatma Gandhi University, India. He received his Ph.D. in 1987 in Polymer Engineering from the Indian Institute of Technology (IIT), Kharagpur, India. He is a fellow of the Royal Society of Chemistry, London and a member of the American Chemical Society. Prof. Thomas's research includes: polymer blends, fiber-filled polymer composites, particulate-filled polymer composites and their morphological characterization, ageing and degradation, pervaporation phenomena, sorption and diffusion, interpenetrating polymer systems, recyclability and reuse of waste plastics and rubbers, elastomer crosslinking, and dual porous nanocomposite scaffolds for tissue engineering.

Dr. Nandakumar Kalarikkal is Associate Professor and Head of the Advanced Materials Laboratory, School of Pure and Applied Physics Member Senate, as well as the International and Inter University Centre for Nanoscience, at Mahatma Gandhi University, India. He received his Ph.D. in Semiconductor Physics at the Cochin University of Science & Technology, Kerala, India and was a postdoctoral fellow at the CSIR-National Institute for Interdisciplinary Science and Technology, Thiruvananthapuram, Kerala, India. Dr. Nandakumar Kalarikkal's research specializes in polymers, which includes synthesis, characterization, and applications of various nanomaterials, ion irradiation effects on various novel materials, and phase transitions.

Related Titles

- Li and Meng, Recent Advances in Smart Self-healing Polymers and Nanocomposites, 2015, 978-1-78242-280-8
- Mittal, Manufacturing Nanocomposites with Engineering Plastics, 2015, 978-1-78242-308-9
- Ray, Environmentally-friendly Polymer Nanocomposites, 2013, 978-0-85709-777-4
- Gao, Advances in Polymer Nanocomposites, 2012, 978-1-84569-940-6
- McNally and Potschke, Polymer-carbon Nanotube Composites, 2011, 978-1-84569-761-7

ISBN 978-0-08-101991-7

9 780081 019917

WP
WOODHEAD PUBLISHING
An imprint of Elsevier
elsevier.com/books-and-journals

ELSEVIER